Department of Physics and Astronomy
University of Heidelberg

Bachelor Thesis in Physics
submitted by

Nikita Schmal

born in Heilbronn (Germany)

2020

Effect of feeddown contributions on blast-wave descriptions of elliptic flow and particle spectra data in heavy ion collisions

This Bachelor Thesis has been carried out by Nikita Schmal at the
Physikalisches Institut Heidelberg
under the supervision of
Prof. Klaus Reygers

Abstract

In this thesis the effect of feeddown contributions from short lived resonances on the simultaneous blast-wave description of particle spectra and elliptic flow is studied. Two different version of the blast-wave model, called the *boost* and *fos* model, were used to fit data from heavy ion collisions at $\sqrt{s_{NN}} = 11.5, 200$ and 2760 GeV.

The results from the simultaneous fits using the *fos* blast-wave model show that feeddown contributions have only a small effect on the shape of the particle spectra and the elliptic flow.

To improve the descriptions of pions at low transverse momenta the same fits were performed using the *boost* blast-wave model which was then able to properly describe the entire pion spectrum for the first time while also describing the other particles just as well as the *fos* model.

Zusammenfassung

In dieser Arbeit wird der Effekt von feeddown von kurzlebigen Resonanzen auf die simultane Beschreibung von Teilchenspektren und elliptischem Fluss mit dem blast-wave Modell untersucht. Dafür werden zwei verschiedene Versionen des blast-wave Modells, bezeichnet als *boost* und *fos* Modell, verwendet um Daten von Schwerionenkollisionen bei $\sqrt{s_{NN}} = 11.5, 200$ und 2760 GeV zu fitten.

Die Ergebnisse des simultanen fits des *fos* blast-wave Modells zeigen, dass die Beiträge von feeddown nur einen kleinen Einfluss auf die Form der Teilchenspektren und den elliptischen Fluss haben. Um eine bessere Beschreibung des Pionen Spektrums zu erhalten wurden die selben fits ein weiteres mal mit dem *boost* blast-wave Modell durchgeführt, wodurch es nun zum ersten mal möglich war das komplette Pionen Spektrum zu beschreiben während alle anderen Teilchen noch genau so gut beschrieben wurden wie mit dem *fos* Modell.

Contents

1 Introduction

The European Organization for Nuclear Research (CERN) is home to the world's most powerful particle accelerator, the **L**arge **H**adron **C**ollider (LHC) specifically designed to find evidence for the Higgs boson [1, 2] and study physics beyond the Standard Model [3].
To do this four different particle detectors have been set up in four separate locations of the accelerator ring: ATLAS, LHCb, CMS and ALICE.
A Large **I**on **C**ollider **E**xperiment (ALICE) is a dedicated heavy-ion particle detector designed to study a state of strongly interacting matter created after the collision of heavy nuclei known as the quark-gluon plasma in which quarks and gluons are quasi deconfined and is believed to be the state the universe was in shortly after the Big Bang [4]. Interactions within this state of matter are predominantly strong allowing one to gain deeper insight into the theory of the strong interaction, namely the theory of Quantum Chromo Dynamics, and the evolution of the early universe by studying it. Due to the short lifetime of this state of matter one has to rely on indirect signatures to study the early stages of the QGP. For this reason, various properties of the QGP are being studied including the transverse momentum spectra of different particles which provide information about the system when it reaches kinetic freeze-out as well as the elliptic flow v_2 describing the anisotropic flow of the medium [5, 6].
One of the models used to describe these hadron spectra is the blast-wave model [7, 8], it is able to describe the hadron spectra of different particles and provides information on the collective radial velocity as well as the kinetic freeze-out temperature of the quark-gluon plasma and is also used to describe the elliptic flow of different particles [6, 9, 10]. The main assumptions made by this model are local thermal equilibrium and a radial expansion of the medium boosting the individual thermal sources as well as instantaneous freeze-out in radial direction.
Although this blast-wave model is frequently used to describe particle spectra [5, 11–13] a proper physical interpretation of the resulting fit parameters requires multiple particle spectra to be described simultaneously. In these previous studies the blast-wave model was not able to describe the spectra of pions properly especially at lower transverse momenta which is why pions are excluded from most of these fits. These differences at low p_T are usually attributed to feeddown from resonance decays i.e. decays of the form $\eta \rightarrow \pi^+\pi^-\pi^0$ or $\rho \rightarrow \pi\pi$ where the measured particles are produced in secondary decays and not in the thermal source itself and as such aren't described by the blast-wave model.
In this thesis the effect of feeddown on particle spectra and the elliptic flow v_2 is analyzed using a modified version of the blast-wave model to perform simultaneous fits to particle spectra and their elliptic flow v_2 for energies in the range of $\sqrt{s_{NN}} = 11.5$ GeV $-$ 2.76 TeV.
Additionally, a second modified version of the blast-wave model, called the *boost* blast-wave model, is studied to see if it can provide a better description of the different particle spectra.
Before this is done, however, important properties of the quark-gluon plasma will first be discussed after which a more detailed look into the different versions of the blast-wave model and the calculation of feeddown contributions is taken in Chapter **2**.

1.1 The Quark-Gluon Plasma (QGP)

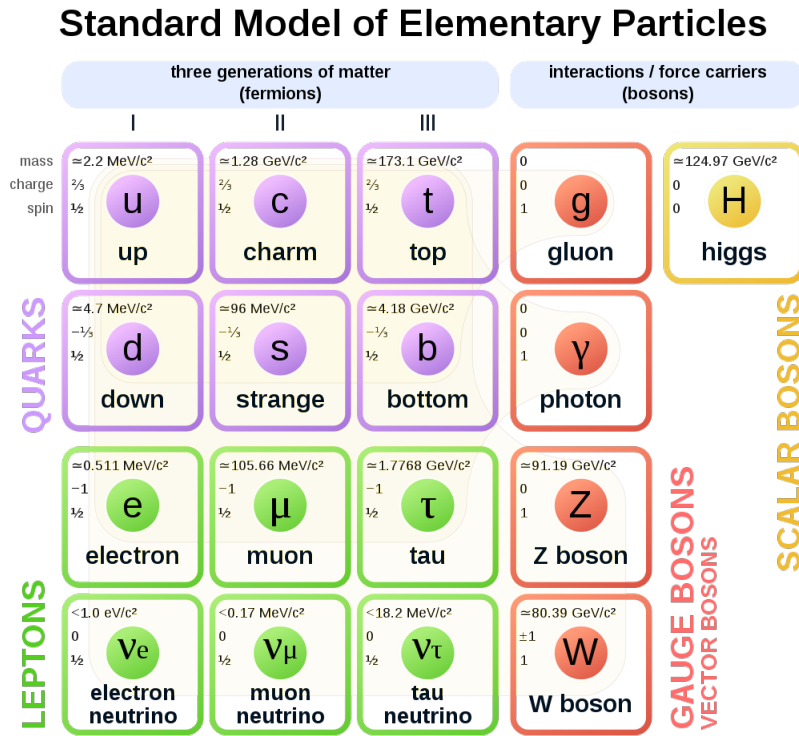**Standard Model of Elementary Particles**

Figure 1: List of elementary particles in the Standard Model of particle physics [14].

In the Standard Model of particle physics the quarks are elementary particles carrying an electric charge as well as one of three different color charges whose interaction with one another is described by the theory of the strong interaction known as **Q**uantum **C**hromo **D**ynamics (QCD). This interaction is mediated by the exchange of gluons which also carry their own color charge resulting in QCD being very different from **Q**uantum **E**lectro **D**ynamics (QED) in which electrically neutral photons are exchanged.

This has as a consequence that quarks cannot occur freely in nature since the strength of the strong interaction increases when trying to pull the individual quarks apart forcing them to be confined within hadrons that appear to be colorless to the outside [15].

At sufficiently high temperatures or densities, however, particles are packed together so tightly that the individual quarks aren't able to distinguish which of the different quarks was their initial 'partner' anymore resulting in a strongly interacting state of matter known as quark-gluon plasma in which quarks and gluons are freed from confinement [16].

Since these high energies densities rarely occur naturally an intense experimental effort was required to be able to properly study its properties leading to the construction of particle accelerators that are able to collide heavy nuclei at very high center of mass energies allowing one to finally reach the energy densities needed to form the QGP.

1.2 QGP in Heavy ion collisions

1.2.1 Space-time evolution of the QGP

Ultra-relativistic heavy ion collisions are a great experimental tool to create and study the QGP under controlled conditions allowing us to probe the matter at different stages of its evolution.
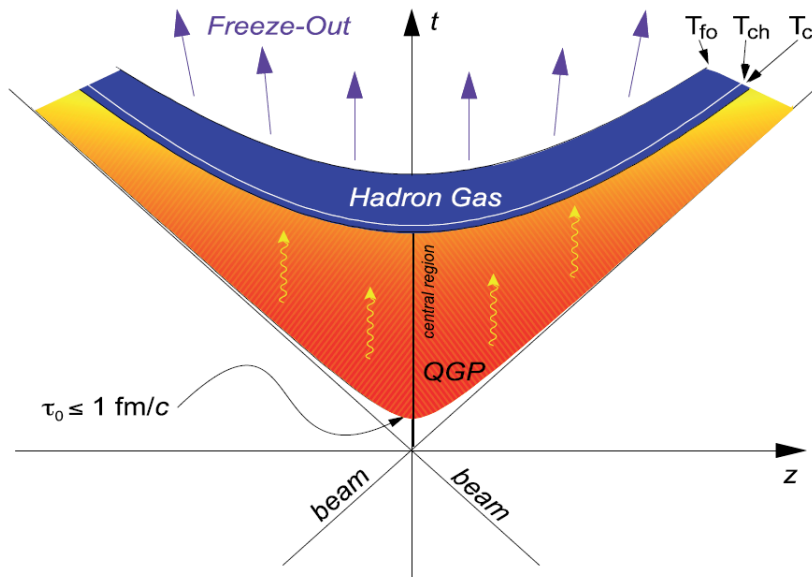

Figure 2: Space-time evolution of ultra-relativistic heavy-ion collisions [17].

In Figure **2** one can see the space-time evolution after the collision of heavy ions which can be split up into different stages:

1.) Immediately after the collision in the pre-equilibrium phase the quarks and gluons are completely liberated until the quarks and gluons start to rapidly thermalize creating the QGP.

2.) After this initial thermalization the QGP begins to expand and cools down until the chemical freeze-out temperature of approximately 155 MeV [18] is reached at which point the inelastic reactions cease and the particle yields from the thermal source are fixed.

3.) The hadron gas then continues expanding until it reaches its kinetic freeze-out temperature where the elastic reactions cease as well and all particles now freely stream to the detectors.

1.2.2 Centrality of the collision

Since we are looking at the collision of two nuclei which naturally are extended objects it is necessary to take the collision geometry into account.

Due to their high speed the nuclei are Lorentz contracted along the beam axis which makes them appear flat in the laboratories frame of reference. The nuclei can overlap almost completely for a head-on collision with a high number of participating nucleons or just have a very slight overlap for peripheral collisions and a low number of participating nucleons.

These geometric properties are described by the centrality which is divided into several different intervals between 0-100% with smaller percentages describing more central collisions.

1.2.3 Experimental observables

In this thesis we are interested in two different experimental observables, the first one being the transverse momentum spectra of the individual particles. These are of particular interest since their behavior at low p_T reflects the properties of the bulk medium at kinetic freeze-out which makes it possible to study its collective behavior.

It is expected that, if the fireball after the collision contained a QGP, the pressure gradients would lead to a collective radial expansion. To extract information on the radial flow velocity and the temperature of the medium theoretical models have to be used to describe the hadron spectra which in our case will be the so called blast-wave model that will be discussed further in the following chapter **2**.

It was previously mentioned that the collision does not necessarily need to be perfectly central resulting in an almond-shaped overlap region of the nuclei i.e. an initial spatial azimuthal anisotropy which develops into a momentum anisotropy over time and can then be measured as an azimuthal anisotropy in particle production [19]. This anisotropy can be expressed by the coefficients of the Fourier expansion of the azimuthal dependence of the particle yields [20] where the elliptic flow is defined as the second of these Fourier coefficients:

$$E\frac{d^3N}{d^3p} = \frac{1}{2\pi}\frac{d^2N}{p_T dp_T dy}(1 + \sum_{n=1}^{\infty} 2v_n \cos(n(\phi - \Psi_r)))$$ (1.1)

where Ψ_r denotes the reaction plane angle which can either be measured directly or indirectly requiring it to be estimated using other means that are explained in more detail in [21].

Measurements of this elliptic flow are an important probe for the early stages of the collision since the momentum anisotropy of the system mostly develops at this stage. In addition, the elliptic flow gives insight into the thermalization process since a large v_2 indicates that the particles took part in the collective flow. Furthermore, the measured elliptic flow provides an estimator of the thermalization time scale since delayed thermalization would lead to a decrease of the initial spatial deformation due to free-streaming and as such would decrease the elliptic flow [22].

2 The Blast-wave model and feeddown

2.1 History of the blast-wave model

The blast-wave model is a theoretical model developed in 1993 by Schnedermann *et al* [7, 8] to describe the measured hadron spectra from heavy ion collisions.

In this model it was assumed that all particles are produced from a Boltzmann distributed thermal source with the following transverse velocity profile:

$$\beta_T(r) = \beta_s \left(\frac{r}{R} \right)^n \tag{2.1}$$

with the radial distance r from the center of the fireball with radius R, the surface velocity β_s and the parameter n to vary the form of the profile.

The resulting particle spectrum is then given as the superposition of the individual thermal components boosted with the boost angle $\rho = \tanh^{-1}(\beta_T)$:

$$\frac{dn}{m_\mathrm{T} dm_\mathrm{T}} \propto \int_0^R r dr m_\mathrm{T} I_0 \left(\frac{p_\mathrm{T} \sinh(\rho)}{T} \right) K_1 \left(\frac{m_\mathrm{T} \cosh(\rho)}{T} \right) \tag{2.2}$$

where both I_0 and K_1 are modified Bessel functions, p_T the transverse momentum and m_T the transverse mass given as $m_T = \sqrt{p_T^2 + m^2}$ with rest mass m.

Here $T = T_{kin}$ describes the kinetic freeze-out temperature since this model describes the fixed hadron spectra post freeze-out and assumes an azimuthally symmetric freeze-out surface.

This model already provided a good description for different hadron spectra using the kinetic freeze-out temperature T_{kin} and the strength of the radial flow as the only two parameters.

This parametrization, however, only described central collisions and was modified in [23] to take the azimuthal modulation of the collective radial flow into account deriving a compact formula for v_2 in the process and was then generalized even further in [9] by adding an additional parameter s_2 to describe the variation of azimuthal density in the source element which then lead to the following formula for the elliptic flow:

$$v_2(p_T) = \frac{\int_0^{2\pi} d\phi_s \cos(2\phi_s) \, I_2(\xi_p) \, K_1(\xi_m) \, (1 + 2s_2\cos(2\phi_b))}{\int_0^{2\pi} d\phi_s \, I_0(\xi_p) \, K_1(\xi_m) \, (1 + 2s_2\cos(2\phi_b))} \tag{2.3}$$

with

$$\xi_p(\phi_s) = \frac{p_T}{T}\sinh(\rho(\phi_s)) \qquad \xi_m(\phi_s) = \frac{m_T}{T}\cosh(\rho(\phi_s)) \tag{2.4}$$

and ϕ_s, ϕ_b describe the azimuthal angle in coordinate or momentum space respectively.

This formula has been used successfully by the STAR collaboration to fit the measured elliptic flow data [24] providing a good description for hadrons at varying center-of-mass energies.

In [25] a radial dependence of the flow velocity was then introduced into the expression for v_2 which will be further generalized in the description used in this thesis as seen in the next section.

2.2 Blast-wave model for an elliptic freeze-out-surface

In this thesis we use a compact formula for the elliptic flow v_2 and the particle yield as presented in [26] where an elliptical freeze-out surface was assumed with the boost-vector of a source element ϕ_b perpendicular to the elliptical sub-shell it is found on, as suggested in [27]. These are described with the angles ϕ_s and ϕ_b as illustrated in Figure **3**.
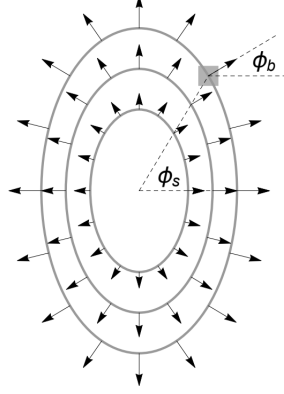

Figure 3: Elliptical freeze-out surface illustrating the angles ϕ_s and ϕ_b[26].

The position of a source element is then described by introducing the variables $\hat{r}$ and $\hat{\phi}$:

$$x = R_x \hat{r} \cos \hat{\phi}, \qquad y = R_y \hat{r} \sin \hat{\phi} \tag{2.5}$$

with R_x and R_y describing the radii of the ellipse along the x- and y-axis.
This then gives the following relations for the different angles:

$$\tan \phi_b = \frac{R_x^2}{R_y^2} \tan \phi_s = \frac{R_x}{R_y} \tan \hat{\phi} \tag{2.6}$$

With this the invariant particle yield averaged over the azimuthal angle ϕ_p is then:

$$\frac{1}{2\pi p_T} \frac{\mathrm{d}N}{\mathrm{d}p_T \mathrm{d}y} \propto m_T \int\limits_0^1 \hat{r}\mathrm{d}\hat{r} \int\limits_0^{2\pi} \mathrm{d}\hat{\phi} \, I_0(\xi_p)K_1(\xi_m) \tag{2.7}$$

where both $\xi_{p/m}$ are the same as above with the radial velocity profile:

$$\rho \equiv \rho(\hat{r}, \hat{\phi}) = \hat{r} \left(\rho_0 + \rho_2 \cos(2\phi_b) \right) \tag{2.8}$$

$$\phi_b \equiv \phi_b(\hat{\phi}) = \arctan \left(\frac{R_x}{R_y} \tan \hat{\phi} \right) + \lfloor \frac{\hat{\phi}}{\pi} + \frac{1}{2} \rceil \pi \tag{2.9}$$

and $\lfloor x \rceil$ denotes the greatest integer less than or equal to x.
From this an expression for the elliptic flow can then be obtained by taking the average of $\cos(2\phi_p)$ over the azimuthal particle distribution:

$$v_2(p_T) = \frac{\int_0^1 \hat{r}\mathrm{d}\hat{r} \int_0^{2\pi} \mathrm{d}\hat{\phi} \, \cos(2\phi_b)I_2(\xi_p)K_1(\xi_m)}{\int_0^1 \hat{r}\mathrm{d}\hat{r} \int_0^{2\pi} \mathrm{d}\hat{\phi} \, I_0(\xi_p)K_1(\xi_m)}. \tag{2.10}$$

2.3 The *boost* blast-wave model

In addition to the previous version of the blast-wave model which will simply be referred to as the *fos* model (Freeze-out-surface) we also want to make use of a different model that doesn't explicitly reference any specific freeze-out surface following [28].

In this case we make use of the Lorentz invariance of d^3p/E and assume that in the rest frame of the source, labeled as d^3p^*/E^*, the momenta of the particles are thermally distributed.

A particle with four-momentum p in the rest frame has the energy $E^* = p \cdot u$ which gives us:

$$E\frac{d^3N}{d^3p} = E^*\frac{d^3N}{d^3p^*} \propto p \cdot u e^{-p \cdot u/T} \tag{2.11}$$

with the four velocity of the fluid cell u.

The contribution of all source elements can then be added up by integrating over both the longitudinal space-time rapidity η and their transverse positions described by $\hat{r}$ and $\hat{\phi}$ assuming longitudinal boost invariance:

$$E\frac{d^3N}{d^3p} \propto \int_0^1 \hat{r}\, d\hat{r} \int_0^{2\pi} \hat{\phi}\, d\hat{\phi} \int_{-\infty}^{\infty} d\eta\; p \cdot u e^{-p \cdot u/T} \tag{2.12}$$

The integration over the particle azimuthal angle ϕ_p and space-time rapidity η can then be performed analytically and finally leads to the invariant yield:

$$\frac{1}{2\pi p_T}\frac{dN}{dp_T dy} \propto \int_0^1 \hat{r}\, d\hat{r} \int_0^{2\pi} d\hat{\phi}\; T[\xi_m I_0(\xi_p)K_1(\xi_m) - \xi_p I_1(\xi_p)K_0(\xi_m)] \tag{2.13}$$

From this we can then once again derive a formula for the elliptic flow:

$$v_2(p_T) = \frac{\int_0^1 \hat{r}d\hat{r} \int_0^{2\pi} d\hat{\phi}\; \cos 2\phi_b[2I_2(\xi_p)K_0(\xi_m) + \xi_m I_2(\xi_p)K_1(\xi_m) - \xi_p I_1(\xi_p)K_0(\xi_m)]}{\int_0^1 \hat{r}d\hat{r} \int_0^{2\pi} d\hat{\phi}\; [\xi_m I_0(\xi_p)K_1(\xi_m) - \xi_p I_1(\xi_p)K_0(\xi_m)]} \tag{2.14}$$

Unlike the previous model this version of the blast-wave model now takes particles that are emitted into the opposite direction of the thermal source into account which should possibly allow one to get a better description of the pions at low p_T.

From now on this version of the blast-wave model will be referred to as the *boost* model to make it easier to distinguish the two versions from one another.

2.4 Calculating feeddown contributions

As discussed in the previous section, the blast-wave model describes the particle yields one would measure if all particles freely stream to the detectors post freeze-out. This obviously is not the case though since a lot of the particles decay in the time it takes for them to reach the detectors affecting the measured particle yields especially for lighter particles which are at the end of most decay chains e.g. pions.

In this section we want to describe the method used to determine the feeddown for both the transverse momentum spectra and the elliptic flow v_2 for all particle species.

2.4.1 Feeddown contributions to particle yields

Our goal is to determine the feeddown for some particle species that we'll label with d.

To do this we consider a mother particle m that is able to decay to d and define $f^{m \to d}$ to describe the feeddown contribution of one mother particle species m to the daughter particle d allowing one to write the total feeddown for a certain p_T as:

$$f_d(p_T) = \sum_m f^{m \to d}(p_T) \tag{2.15}$$

by summing over all possible mother particles m.

If we assume the total number of mother particles to be $\tilde{N}_m$ we can define the particle yield:

$$f_m(\tilde{p}_T) = \left. \frac{d\tilde{N}_m}{d\tilde{p}_T d\tilde{y}} \right|_{\tilde{y}=0} \tag{2.16}$$

Each of these mother particles has a certain transverse momentum $\tilde{p}_T$ and can then decay to our particle of interest d with a transverse momentum p_T resulting from the decay process.

We now define decay maps $g^{m \to d}(p_T, \tilde{p}_T)$ that describe the normalized invariant yield of the daughter particle d as a function of both the transverse momentum of the mother $\tilde{p}_T$ and the daughter p_T. Using this we can then write the feeddown contribution of a mother m as:

$$f^{m \to d}(p_T, \tilde{p}_T) = g^{m \to d}(p_T, \tilde{p}_T) f_m^{prim}(\tilde{p}_T) \tag{2.17}$$

where f_m^{prim} is the particle yield of the primary mother particles.

To get the total feeddown from the mother particle m we then simply have to integrate over all possible transverse momenta $\tilde{p}_T$ of the mother:

$$f^{m \to d}(p_T) = \int_0^\infty g^{m \to d}(p_T, \tilde{p}_T) f_m^{prim}(\tilde{p}_T) d\tilde{p}_T \tag{2.18}$$

To determine the feeddown contributions of the different particles we need a way to calculate the decay maps $g^{m \to d}(p_T, \tilde{p}_T)$.

To do this the Pythia 8 [29, 30] event generator has been used to simulate the decays of the mother particles considering all particles up to a mass of 2 GeV/c^2 [28]. They are uniformly distributed with rapidities in the range $y_{max} = \pm 1.2$ and p_T from 0 to 20 GeV/c considering only decays of particles with a lifetime $c\tau < 1$fm.

The decay map of a daughter particle d from a mother m can then be written as:

$$g^{m \to d}(p_T, \tilde{p}_T) = \frac{1}{f_m^{gen}(\tilde{p}_T)} \int_{-\tilde{y}_{max}}^{\tilde{y}_{max}} \mathrm{d}\tilde{y} \left. \frac{\mathrm{d}N_m^{gen}}{\mathrm{d}p_T \mathrm{d}y \mathrm{d}\tilde{p}_T \mathrm{d}\tilde{y}} \right|_{y=0}, \tag{2.19}$$

where $f_m^{gen}(\tilde{p}_T)$ is the generated flat $\tilde{p}_T$ spectrum of the mother particle.

All decay particles from this simulation are then put into a histogram counting the number of daughter particles with transverse momentum p_T from a mother particle with transverse momentum $\tilde{p}_T$ as shown in Figure 4 for the case of η to π^- decays.
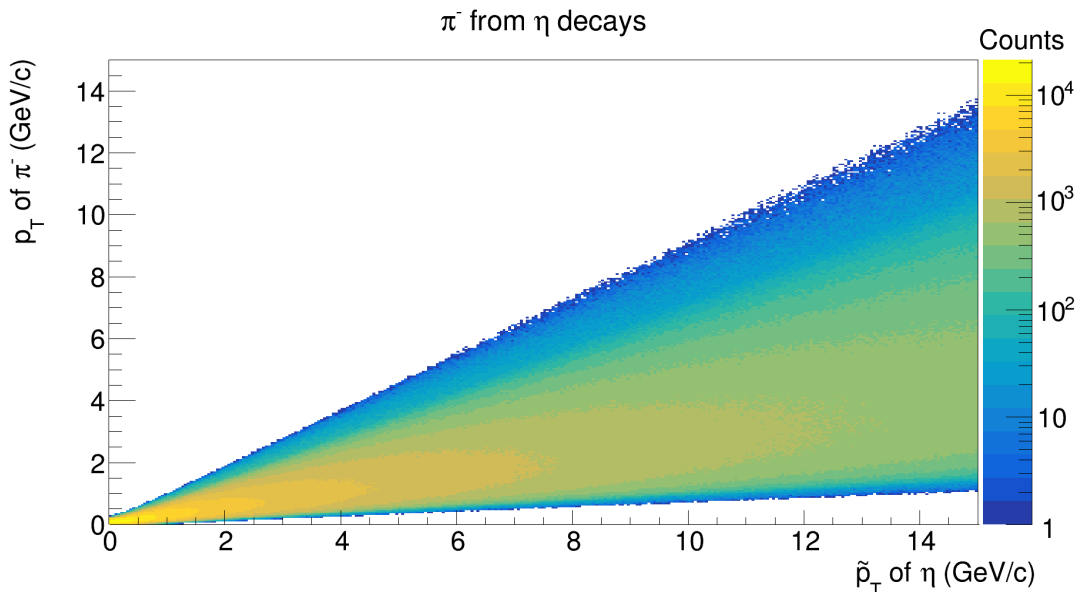

Figure 4: Exemplary histogram depicting the number of π^- created from η decays.

To calculate the feeddown at the p_T from one mother for a specific daughter particle we now get the number of decay particles at p_T from mothers with $\tilde{p}_T$ using the respective histogram and divide this value by the yield of the generated mother particles with $\tilde{p}_T$ to get the $g^{m \to d}(p_T, \tilde{p}_T)$. As shown in equation (2.17) we then need to calculate the particle yield of the primary mother particle which is done using the formula of one of our two blast-wave models.

We assume these particle yields to be proportional to the equilibrium densities:

$$n_i = \frac{g_i}{2\pi^2} T_{ch} m_i^2 K_2\left(\frac{m_i}{T_{ch}}\right) e^{\mu/T_{ch}} \tag{2.20}$$

of a particle species i with mass m_i in a non-interacting hadron gas at temperature T_{ch} and with spin degeneracy g_i which is why the particle yields from the blast-wave model are normalized using these particle densities with $T_{ch} = 155$ MeV and assuming that $\mu \approx 0$.

Using the calculated $g^{m \to d}(p_T, \tilde{p}_T)$ and normalized $f_m^{prim}(\tilde{p}_T)$ the feeddown of a single mother species j can then be calculated using equation (2.18) by repeating this process for all transverse momenta $\tilde{p}_T$ of the mother particle. To get the total feeddown all contributions of the different mother particles are then added up as seen in equation (2.15).

2.4.2 Feeddown contributions to elliptic flow

In the case of elliptic flow (v_2) we take a look at the difference of the azimuthal angles $\Delta\phi = \phi_m - \phi_d$ of our mother m and decay particle d and use this to define:

$$h(\Delta\phi, p_T, \tilde{p}_T) = \frac{\mathrm{d}g^{m\to d}(p_T, \tilde{p}_T)}{\mathrm{d}\Delta\phi} \tag{2.21}$$

With this we can then write:

$$\langle \cos 2\Delta\phi \rangle^{m\to d}(p_T, \tilde{p}_T) := \frac{\int_0^{2\pi} \mathrm{d}\Delta\phi \; \cos(2\Delta\phi) h(\Delta\phi, p_T, \tilde{p}_T)}{\int_0^{2\pi} \mathrm{d}\Delta\phi \; h(\Delta\phi, p_T, \tilde{p}_T)} \tag{2.22}$$

Using the elliptic flow v_2 of the mother particle then allows one to calculate the v_2 of the daughter particle using:

$$v_2^{m\to d}(p_T) = \frac{\int \mathrm{d}\tilde{p}_T \; g^{m\to d}(p_T, \tilde{p}_T) f_m^{prim}(\tilde{p}_T) v_{2,m}^{prim}(\tilde{p}_T) \langle \cos 2\Delta\phi \rangle^{m\to d}(p_T, \tilde{p}_T)}{\int \mathrm{d}\tilde{p}_T \; g^{m\to d}(p_T, \tilde{p}_T) f_m^{prim}(\tilde{p}_T)} \tag{2.23}$$

where $v_2^{prim}(\tilde{p}_T)$ is the calculated elliptic flow of the primary mother particles.

We see that to determine the feeddown contributions to the elliptic flow we need another two-dimensional map $\langle \cos 2\Delta\phi \rangle^{m\to d}(p_T, \tilde{p}_T)$ similar to the decay maps $g^{m\to d}(p_T, \tilde{p}_T)$.

To get these, another set of histograms, using the exact same simulated decays as above, was created in which each of the decay particles were weighted with $\cos(2\Delta\phi)$ or in this case $\cos(2\phi_d)$, with the azimuthal angle of the decay particle ϕ_d, since the azimuthal angles of the mother particles in these simulated decays were set to be $\phi_m = 0$. In Figure **5** one can see the two-dimensional map of $\langle \cos(2\Delta\phi) \rangle$ from the same η to π^- decays as before.
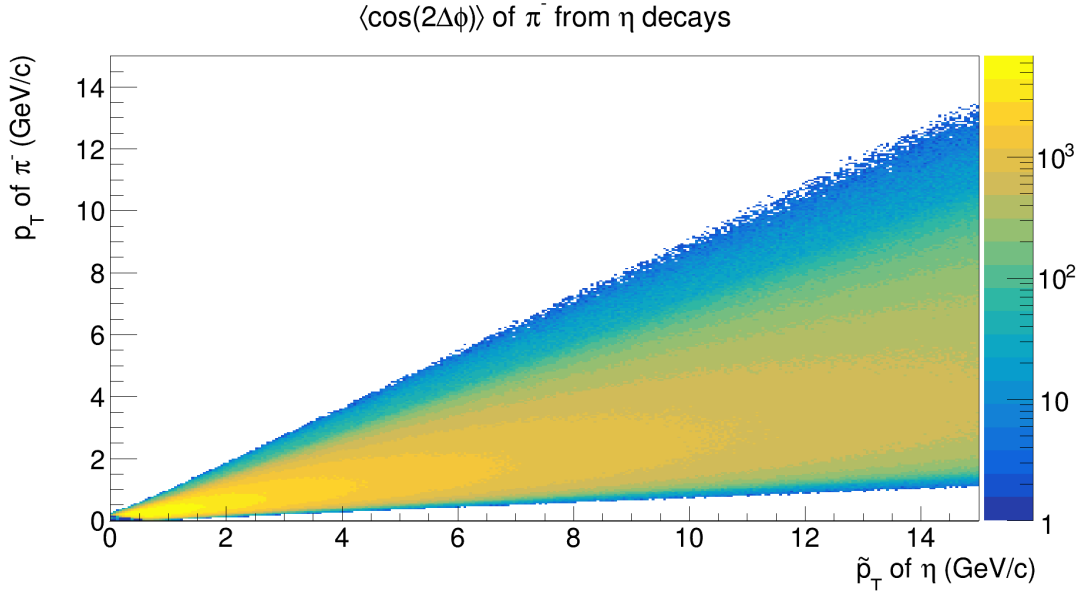

Figure 5: Exemplary histogram of π^- from η decays weighted with $\cos(2\Delta\phi)$.

The total feeddown to a daughter d at a certain p_T can then simply be calculated using:

$$v_{2,d}(p_\mathrm{T}) = \frac{\sum_m f^{m \to d}(p_\mathrm{T}) v_2^{m \to d}(p_\mathrm{T})}{\sum_m f^{m \to d}(p_\mathrm{T})} \tag{2.24}$$

The process to calculate the feeddown contributions to the elliptic flow is then summed up. Once again the normalized particle yield of the primary mothers $f_m^{prim}(\tilde{p}_\mathrm{T})$ and their elliptic flow $v_{2,m}^{prim}(\tilde{p}_\mathrm{T})$ is calculated using the formulas from our blast-wave model. The $g^{m \to d}(p_\mathrm{T}, \tilde{p}_\mathrm{T})$ is then determined just like before and we find the $\langle \cos(2\Delta\phi) \rangle^{m \to d}(p_\mathrm{T}, \tilde{p}_\mathrm{T})$ using the respective two-dimensional map. With all of these values the feeddown contribution to the elliptic flow can then be calculated using (2.23) by once again repeating this for all possible transverse momenta $\tilde{p}_\mathrm{T}$ of the mother. The total feeddown contribution is then given as the sum over all possible mother particles using (2.24).

From this we see that the calculation of the feeddown contribution to the elliptic flow gives one all the necessary values to determine the feeddown to their particle yields making it easy to calculate both the feeddown for particle yields and elliptic flow v_2 at the same time.

Both two-dimensional maps for $g^{m \to d}(p_\mathrm{T}, \tilde{p}_\mathrm{T})$ and $\langle \cos(2\Delta\phi) \rangle^{m \to d}(p_\mathrm{T}, \tilde{p}_\mathrm{T})$, provided by [28], are only calculated once before the actual fit of our spectra which then always use the same maps for all of the different fits that were done.

For these fits one naturally needs the total particle yield and elliptic flow since the experimental data measures both primary particles from the thermal source and those from feeddown contributions. These totals are simply the sum of both feeddown and primary contributions and are calculated with:

$$f_d^{tot}(p_\mathrm{T}) = f_d^{prim}(p_\mathrm{T}) + \sum_m f^{m \to d}(p_\mathrm{T}) \tag{2.25}$$

$$v_{2,d}^{tot}(p_\mathrm{T}) = \frac{f_d^{prim}(p_\mathrm{T}) v_{2,d}^{prim}(p_\mathrm{T}) + \sum_m f^{m \to d}(p_\mathrm{T}) v_2^{m \to d}(p_\mathrm{T})}{f_d^{prim}(p_\mathrm{T}) + \sum_m f^{m \to d}(p_\mathrm{T})} \tag{2.26}$$

3 Feeddown for different flow velocities

Before any fits including feeddown contributions are performed, the behavior of feeddown as a function of p_T for different flow velocities is studied. Since pions are the lightest hadrons they are expected to be affected by feeddown the most which is why the following studies will be performed with π^+ particles as an example.

To do this the ratio of π^+ from η, ρ and Δ decays to primary π^+ from the thermal source are plotted for various flow velocities. This is done using the *fos* version of the blast-wave model by setting $T_{kin} = 0.096$ GeV, $R_x/R_y = 0.829$, $\rho_2 = 0.0 - 0.12$ and varying ρ_0 in the range $[0.0, 1.2]$. The results are plotted in Figure **6** for all of the three particles separately along with the sum of all three particle contributions.
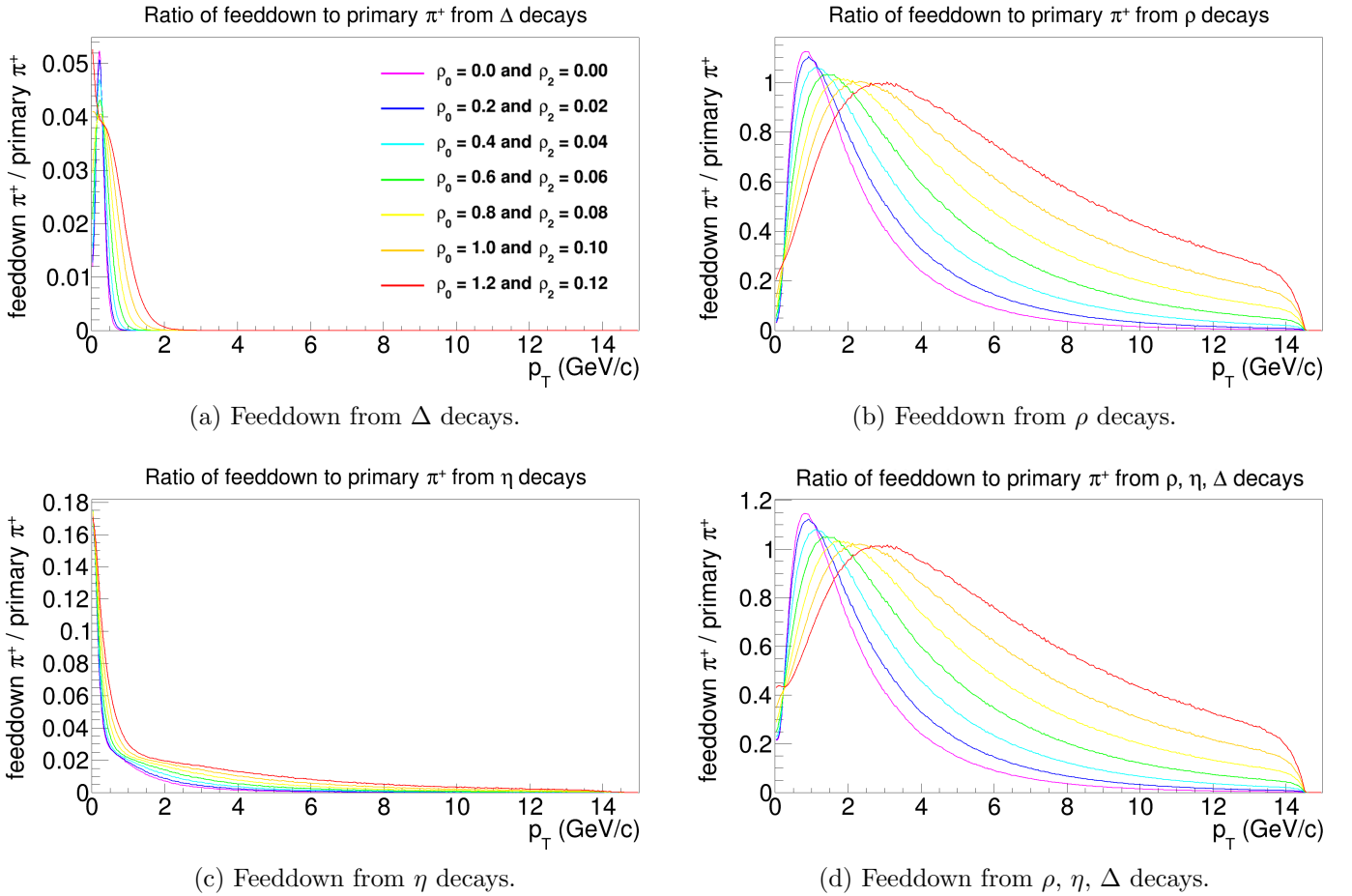

(a) Feeddown from Δ decays.

(b) Feeddown from ρ decays.

(c) Feeddown from η decays.

(d) Feeddown from ρ, η, Δ decays.

Figure 6: Ratio of π^+ from feeddown decays to primary π^+ from the thermal source.

The ratios show a strong dependence of the feeddown contributions on the different flow velocities. At higher flow velocities the feeddown gets boosted to higher values of p_T flattening the curve in the process. Additionally, the feeddown from ρ decays clearly dominate for the feeddown contributions compared to those from η and Δ decays which mostly contribute at very low p_T.

(a) Feeddown from Δ decays.

(b) Feeddown from ρ decays.

(c) Feeddown from η decays.

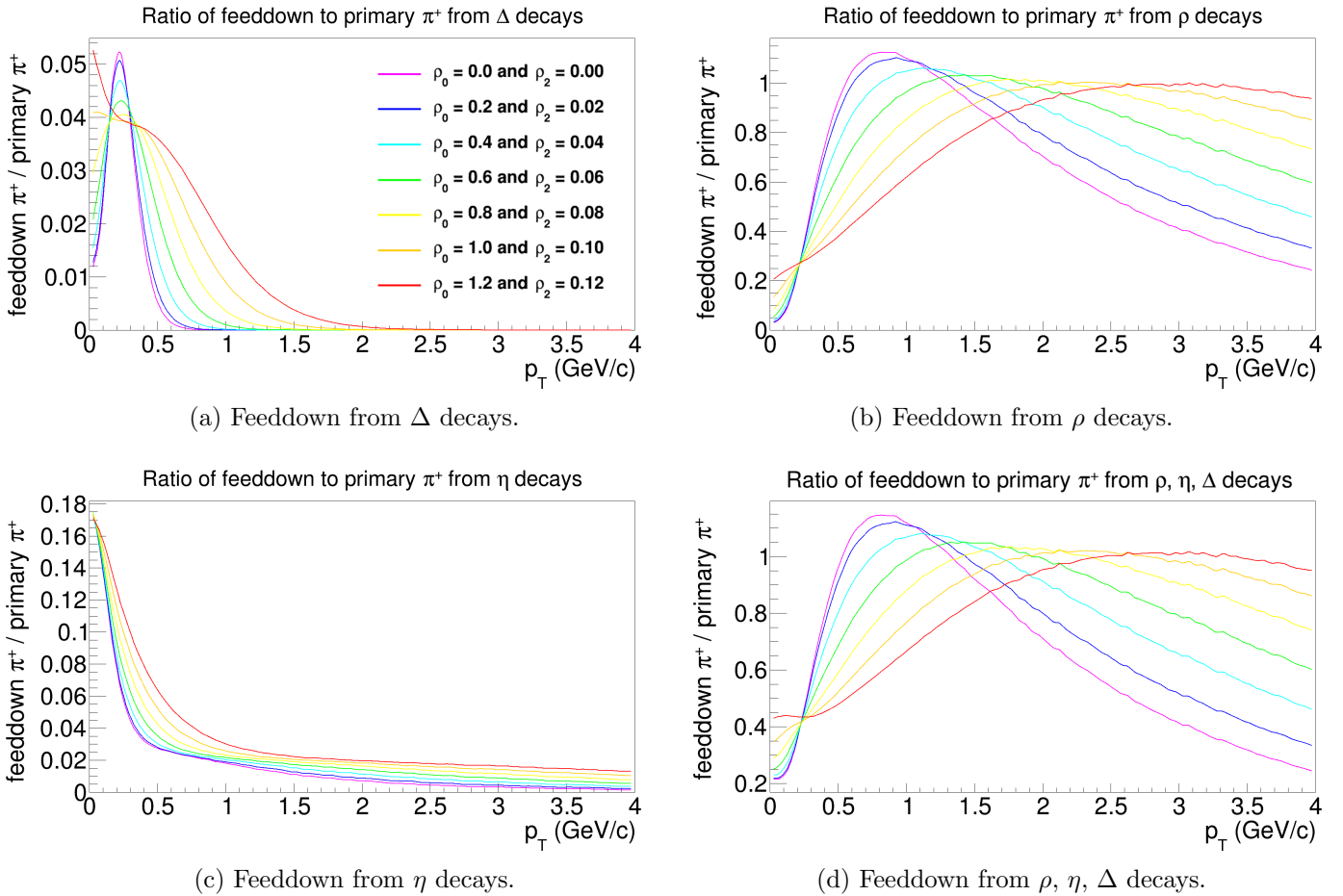(d) Feeddown from ρ, η, Δ decays.

Figure 7: Ratio of π^+ from feeddown decays to primary π^+ from the thermal source.

In Figure **7** the exact same graphs are plotted again, this time restricted to a p_T range up to 4 GeV/c since this allows one to get a better look at the effects of the Δ and η decays. This p_T range also gives better insight into the effect the feeddown has on the particle spectra since it covers the p_T range at which the particle spectra for pions are measured.

The feeddown from η and Δ decays only have significant contributions at $p_\mathrm{T} < 0.5$ GeV/c where they increase the ratios by approximately 0.2 while the rest of the p_T range is dominated by feeddown from ρ decays.

Naturally not all of the feeddown contributions come from ρ, η and Δ decays, hence the same ratio of feeddown to primary particles for all mother particles with a rest mass less than 1.3 GeV/c^2 is plotted in Figure **8**. Additionally, the ratio of primary π^+ to total π^+, i.e. the sum of primary and feeddown, is shown in Figure **9**. Here the maximum rest mass of the mother particles was set to 1.3 GeV/c^2 to make sure that the majority of particles that decay to pions are considered while keeping the computing time reasonably low.
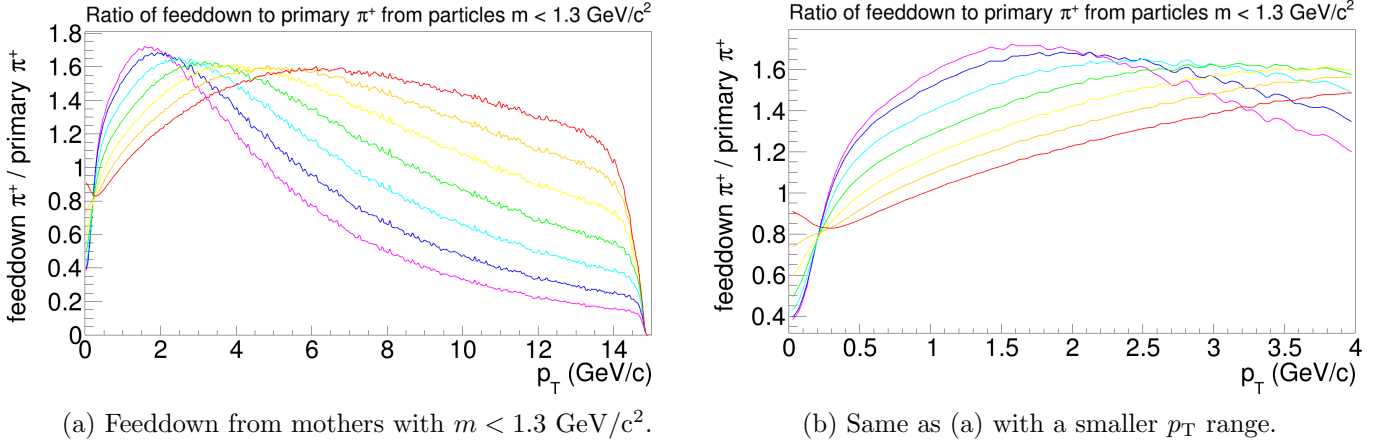
(a) Feeddown from mothers with $m < 1.3 \text{ GeV/c}^2$.

(b) Same as (a) with a smaller p_T range.

Figure 8: Ratio of π^+ from feeddown decays to primary π^+ using the *fos* model.

(a) Feeddown from mothers with $m < 1.3 \text{ GeV/c}^2$.

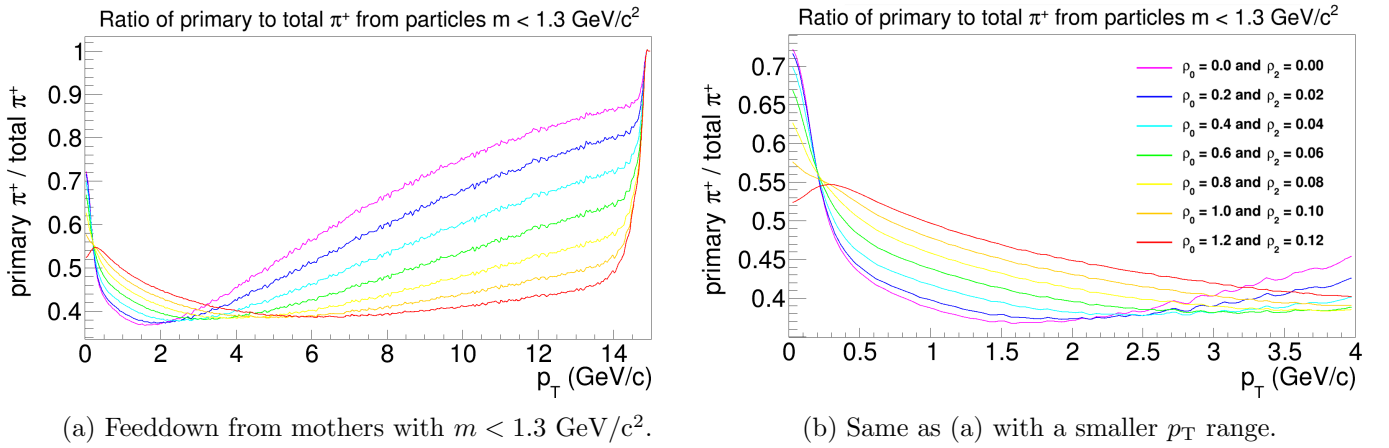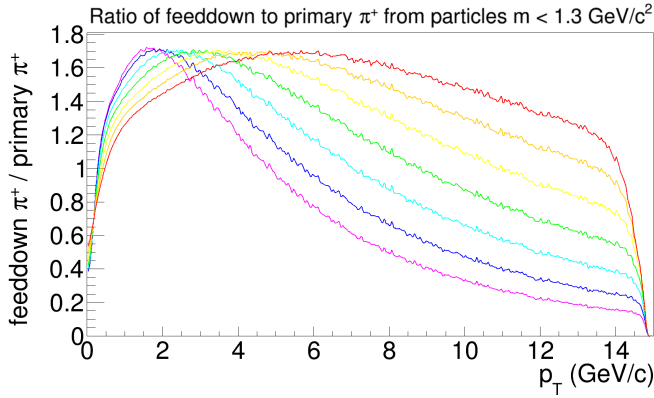(b) Same as (a) with a smaller p_T range.

Figure 9: Ratio of total number of π^+ to primary π^+ using the *fos* model.

From these, one can see that including more mother particles only changes the shape of the ratios slightly while the behavior for different flow velocities stays the same with both of the plotted ratios becoming increasingly flat functions of p_T with higher flow velocities.

In conclusion, the effect of feeddown strongly depends on the respective flow velocity. Since higher flow velocities lead to flatter ratios it is expected that feeddown contributions have less of an effect on the shape of the particle spectra in this case.

Since all of the previous feeddown calculations used the *fos* blast-wave model it is necessary to take a look at the exact same feeddown ratios using the *boost* blast-wave model. The results for the feeddown ratios from mother particles with rest masses lower than 1.3 GeV/c^2 are shown in Figure **10** and **11**.
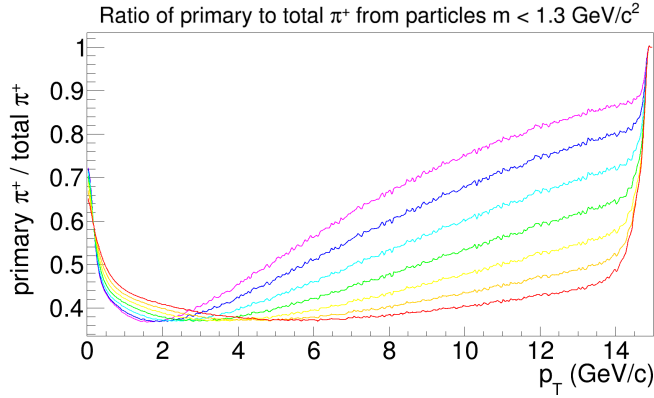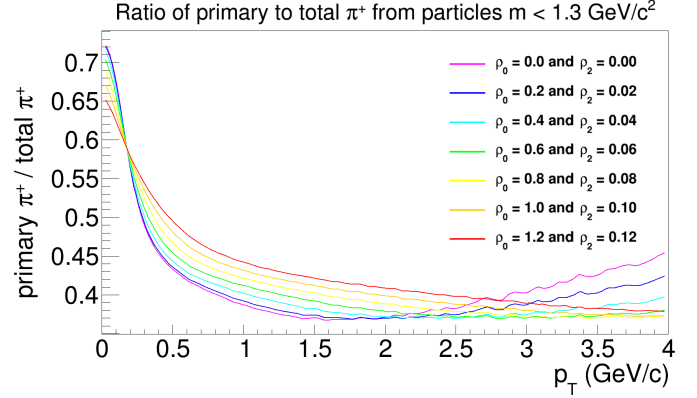
(a) Feeddown from mothers with $m < 1.3$ GeV/c^2.
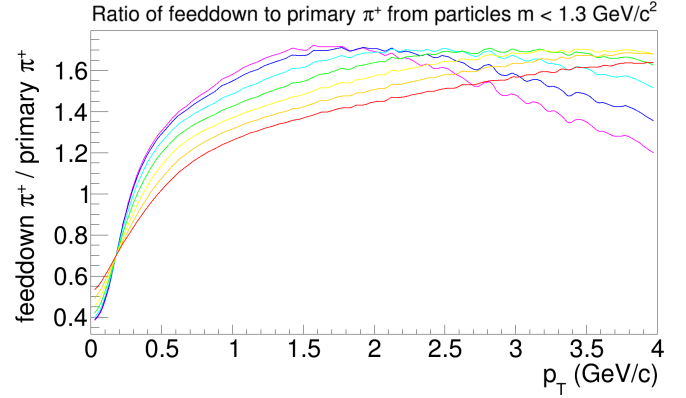
(b) Same as (a) with a smaller p_T range.

Figure 10: Ratio of π^+ from feeddown decays to primary π^+ using the *boost* model.

(a) Feeddown from mothers with $m < 1.3$ GeV/c^2.

(b) Same as (a) with a smaller p_T range.

Figure 11: Ratio of total number of π^+ to primary π^+ using the *boost* model.

Comparing these ratios with those calculated using the *fos* model one can see that both look very similar and also show very similar behavior for increasing flow velocities. The ratios from the *boost* blast-wave model differ the most at low $p_\text{T} < 1$ GeV/c especially for higher flow velocities, possibly improving the description of the low p_T pion spectrum.

Due to the same behavior of the ratios at different flow velocities for both models, all of the properties that have been studied using the *fos* blast-wave model also apply to the feeddown calculated using the *boost* blast-wave model.

4 Simultaneous fits with feeddown

Using the methods described in chapter **2** the simultaneous fits can now be performed. In order to study the effects of feeddown and see how blast-wave fits including feeddown contributions differ from those without, various different fits were performed. At first only the *fos* blast-wave model is considered, simultaneously fitting spectra and elliptic flow for different center of mass energies. For the data analysis the object oriented data analysis framework ROOT [31] was used to perform fits that minimize the χ^2 values using Minuit [32]. All of the fits were done using a GUI which allows one to choose data for different energies and centralities for each individual particle with data provided by an additional tool from [33].

4.1   Simultaneous fits using the *fos* blast-wave model

The first fit was done for data at the center of mass energy $\sqrt{s_{NN}} = 2.76$ TeV at mid-centralities of 30-40%, if available, otherwise the next closest centrality was used. The exact data and centralities used are listed in Table **1** along with the fit ranges of every particle.

The fit ranges were chosen such that the effect of jet contribution, which get more relevant with higher transverse momenta p_T, is minimized by setting the maximum p_T to:

$$p_T^{max} = cm_0\gamma^{max}\beta^{max} + 1.0 \text{ GeV/c} \tag{4.1}$$

with the particle rest mass m_0 and $\beta^{max} = 0.68$.

	π	K	p	ϕ	Ω	D^0	d	J/ψ	Υ
dN/dp_T reference	[34]	[34]	[34]	[35]	[36]	[37]	[38, 39]	[40]	[41]
Centrality (%)	30-40	30-40	30-40	30-40	20-40	30-50	20-40	20-40	0-100
$\sqrt{s_{NN}}$ (TeV)	2.76	2.76	2.76	2.76	2.76	2.76	2.76	5.02	2.76
v_2 reference	[42]	[42]	[42]	[42]	[42]	[43]	[39]	[44]	[45]
Centrality(%)	30-40	30-40	30-40	30-40	20-40	30-50	20-40	20-40	5-60
$\sqrt{s_{NN}}$ (TeV)	2.76	2.76	2.76	2.76	2.76	2.76	2.76	2.76	5.02
p_T fit range (GeV/c)	[0.1,1.4]	[0.1,1.5]	[0.1,1.9]	[0.1,1.9]	[0.1,2.6]	[0.1,2.7]	[0.1,2.7]	[0.1,3.9]	[0.1,9.8]

Table 1: List of used particle data and their respective centralities and energies.

One can see that almost all data was available for $\sqrt{s_{NN}} = 2.76$ TeV Pb-Pb collisions except for the J/ψ particle spectrum and the Υ elliptic flow where the data at 5.02 TeV was used. All of the particle spectra were then normalized to their integral and the systematic and statistical error of each data point was added in quadrature. Figure **12** shows the results of the simultaneous fit for both particle spectra and elliptic flow. The particle spectra plots depict the ranges of the data points used in the simultaneous fit as solid red lines with the predictions from the resulting fit parameters, listed in Table **2**, shown as dashed gray lines. The plots for the elliptic flow similarly depict the range of the fitted particle as a solid colored line with predictions as dashed lines. In this case, however, all lines have the same color as their respective data points to make it easier to distinguish them from one another.
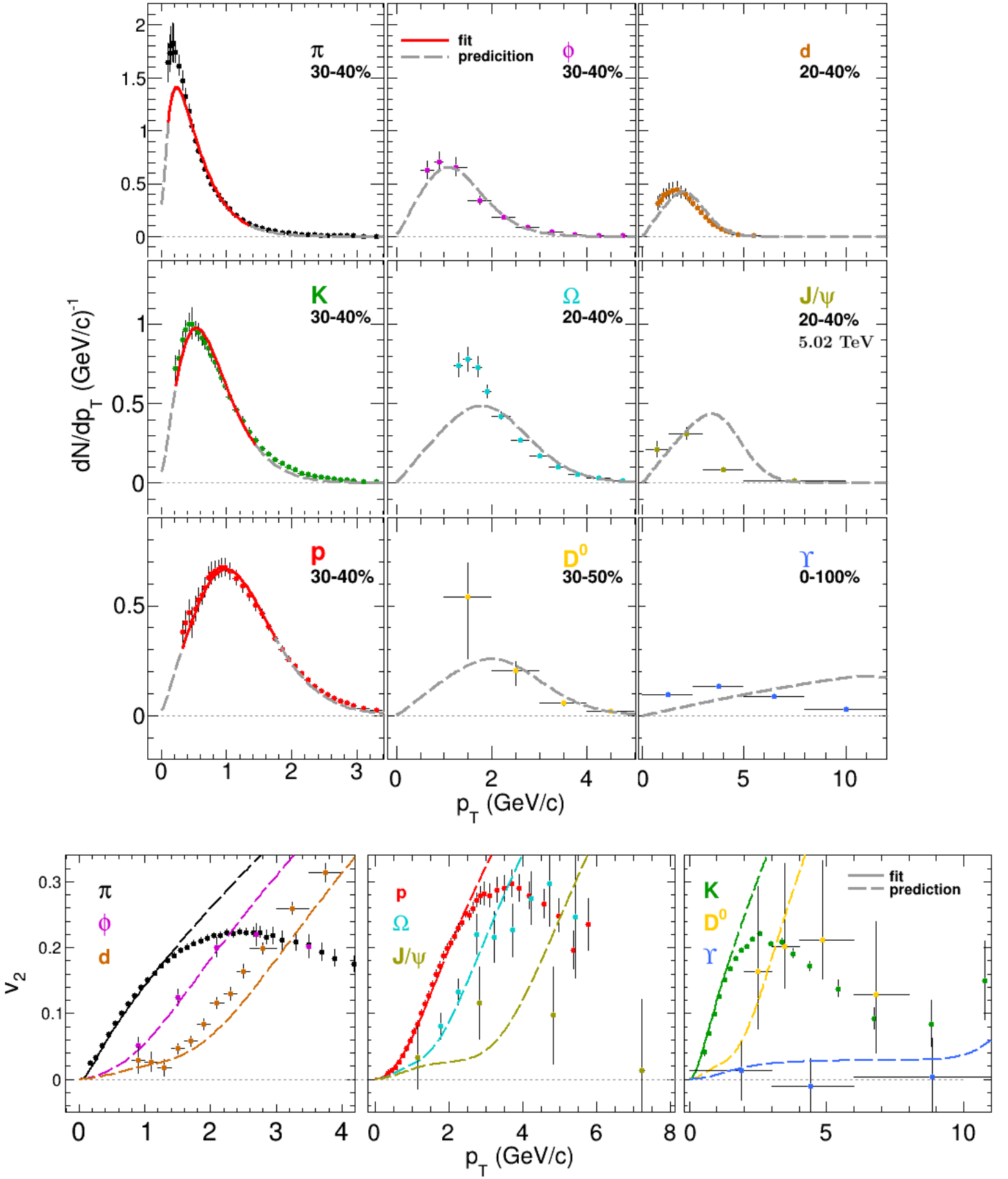
Figure 12: Top: Results of the simultaneous fit for normalized particle spectra using the *fos* blast-wave model. Bottom: Corresponding fit results for the elliptic flow.

Starting from the fits for the particle spectra one can immediately see that most of these spectra are described really well, especially the K, p, ϕ, D^0 and deuterons where all fits describe most data points within their error bars and only a few show deviations slightly greater than one sigma. There are significant deviations of several sigma for the predictions of Ω, J/ψ and Υ where slightly different centralities were used which would at least explain minor differences. Since the Υ spectrum was measured at minimum bias it is also not unexpected that the prediction is not able to describe the data since the fitted particles only used data at centrality 30-40% giving predictions for this centrality.

Looking at the pion spectrum one can see that even when considering feeddown contributions there are still deviations of approximately two sigma at $p_T < 0.5$ GeV/c although it was believed that these deviations are mostly a result of feeddown contributions [6].

The plot for the elliptic flow also shows a good description for almost all particles at low p_T with deviations smaller than one sigma for all data points. It is not expected that the blast-wave model is able to properly describe the elliptic flow at higher p_T since the effect of jet contributions, which are not considered by the blast-wave model in any way, dominates at these transverse momenta. The only particles with slightly larger deviations are the J/ψ which are still described decently when taking the errors into account and the deuterons which are not necessarily expected to be described since they consist of a proton and a neutron making them very different from all the other particles considered here that are only made up of quarks.

This fit allows one to easily see whether or not the *fos* blast-wave model with feeddown is able to describe both particle spectra and elliptic flow properly for all particles and p_T ranges. To further study the effect of feeddown, additional fits that do not take feeddown contributions into account are performed. The resulting fit parameters for fits with- and without feeddown are listed in Table **2** along with the fitted particles. For comparison the same fits excluding the pions was listed as well to see how much of an effect the pions have on the resulting fit parameters when feeddown is considered.

$\sqrt{s_{NN}} = 2.76$ TeV	T_{kin} (GeV)	ρ_0	ρ_2	R_x/R_y
π, K, p with feeddown	0.096 ± 0.014	1.180 ± 0.040	0.075 ± 0.007	0.829 ± 0.008
π, K, p without feeddown	0.106 ± 0.000	1.125 ± 0.005	0.079 ± 0.001	0.831 ± 0.001
K, p with feeddown	0.135 ± 0.007	1.080 ± 0.016	0.097 ± 0.006	0.833 ± 0.004
K, p without feeddown	0.123 ± 0.006	1.079 ± 0.016	0.091 ± 0.006	0.832 ± 0.004

Table 2: Fit parameters from *fos* blast-wave model fits at $\sqrt{s_{NN}} = 2.76$ TeV with- and without feeddown and in- or excluding pions.

Comparing the different values of ρ_2 and R_x/R_y one can see that they only change a little when feeddown is considered while the kinetic freeze-out temperature T_{kin} and flow velocity ρ_0 in- or decrease slightly. In addition, the fits excluding the pions now show an even larger change of the fit parameters then without feeddown contributions.

Since lighter particles are affected by feeddown the most only the particle spectra for pions, kaons and protons will be compared. As can be seen in Figure **13** the difference of fits with- and without feeddown is marginal. To properly visualize the effect of feeddown in detail, the ratio of primary particles from the thermal source and the total particle number i.e. the sum of both feeddown and primary particles is plotted as well.
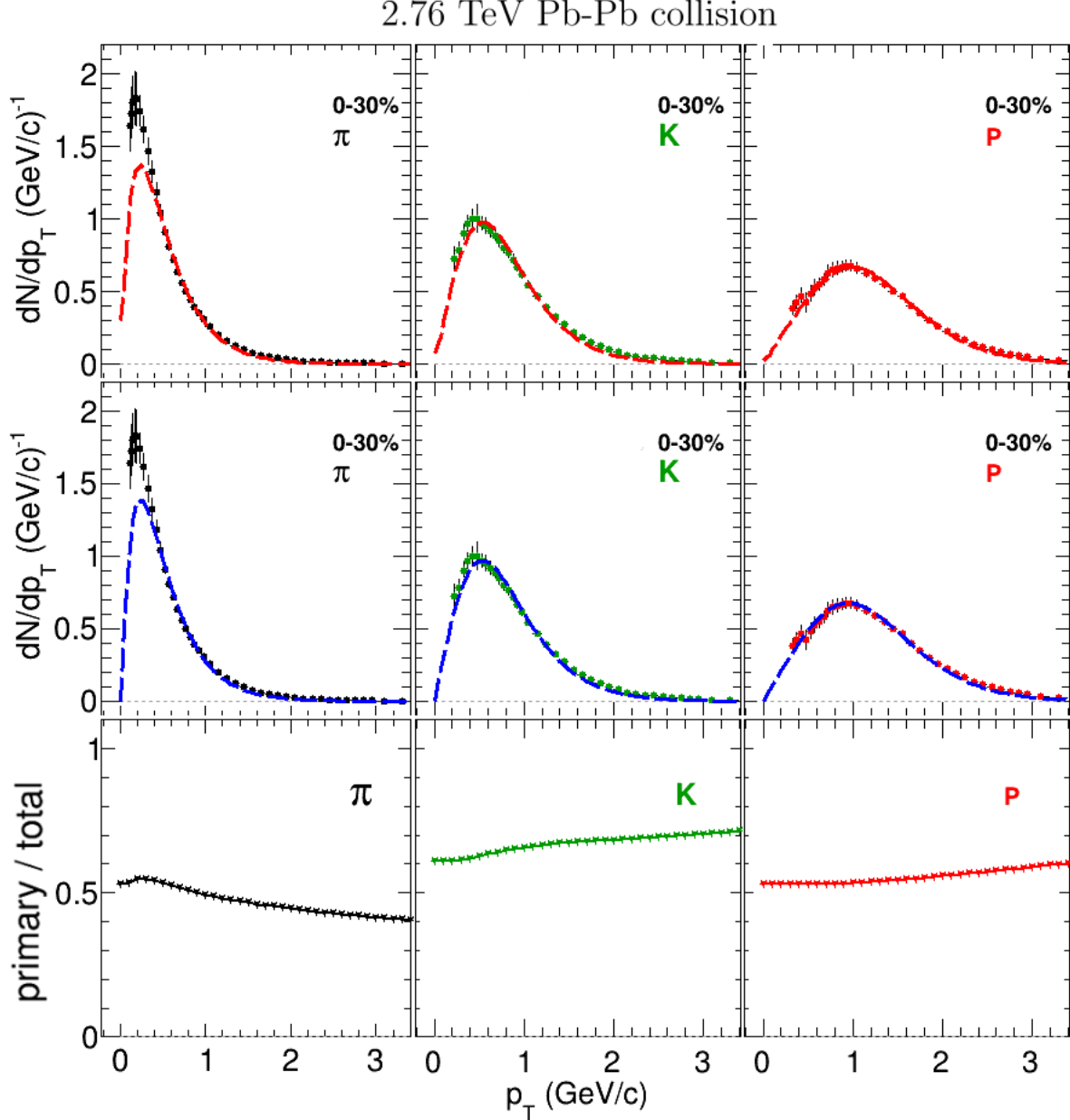

Figure 13: Effect of feeddown on pion, kaon and proton particle spectra at $\sqrt{s_{NN}} = 2.76$ TeV. Top: Feeddown fits. Middle: Non-feeddown fits. Bottom: Ratios of primary to total particles.

The ratio of primary to total particles is a relatively flat function of p_T which only results in minor changes of the spectral shapes. This agrees with the results of Chapter **3** where the effect of feeddown is expected to be small for higher flow velocities like the ones here. Looking at the ratio of pions at lower p_T though, a small peak of approximately 5-10% is visible and as such should affect the description of the low p_T pions if only a little bit.

In Chapter **3** it was shown that the feeddown strongly depends on the flow velocity. In lower energy collisions this flow velocity is lower, hence the effect of feeddown contributions will be studied in more detail for lower energies at $\sqrt{s_{NN}} = 200$ GeV and $\sqrt{s_{NN}} = 11.5$ GeV.

The used data is once again listed in Tables **3** and **4** for energies of 200 GeV and 11.5 GeV respectively, along with the used centralities and fit ranges which have been calculated using equation (4.1) just like before. All of the data was normalized to their integral with quadratic addition of statistical and systematic errors just like in the previous case.

One of the important changes that have to be considered at lower energies is that differences for particles and anti-particles are to be expected [46] due to baryon stopping effects. For this reason all of the following fits will only consider particles although they will still only be labeled as e.g. π for π^- etc.

	π	K	p	ϕ	Ω	D^0	d	J/ψ	Ξ	K_s^0	Λ	Λ_c
dN/dp_T reference	[47]	[48]	[47]	[49]	[50]	[51]	[52]	[53]	[50]	[50]	[50]	[54]
Centrality (%)	20-40	20-40	20-40	30-40	20-40	20-40	20-40	20-40	20-40	20-40	20-40	10-80
v_2 reference	[55]	[55]	[55]	[55]	[55]	[56]	[57]	[58]	[55]	[55]	[55]	n/a
Centrality (%)	0-30	0-30	0-30	0-30	0-30	10-40	0-80	10-40	0-30	0-30	0-30	n/a
p_T fit range (GeV/c)	[0.1,1.1]	[0.1,1.5]	[0.1,1.9]	[0.1,1.9]	[0.1,2.6]	[0.1,3.0]	[0.1,2.7]	[0.1,3.9]	[0.1,2.2]	[0.1,1.5]	[0.1,2.0]	[0.1,3.1]

Table 3: List of used data and centralities from 200 GeV Au-Au collisions.

	π	K	p	ϕ	Ω	d	Ξ	K_s^0	Λ
dN/dp_T reference	[59]	[59]	[59]	[60]	[60]	[52]	[61]	[61]	[61]
Centrality (%)	30-40	30-40	30-40	30-40	0-60	20-40	30-40	30-40	30-40
v_2 reference	[62]	[62]	[62]	[62]	[62]	[57]	[62]	[62]	[62]
Centrality (%)	10-40	10-40	10-40	10-40	10-40	0-80	10-40	10-40	10-40
p_T fit range (GeV/c)	[0.1,1.1]	[0.1,1.5]	[0.1,1.9]	[0.1,1.9]	[0.1,2.6]	[0.1,2.7]	[0.1,2.2]	[0.1,1.5]	[0.1,2.0]

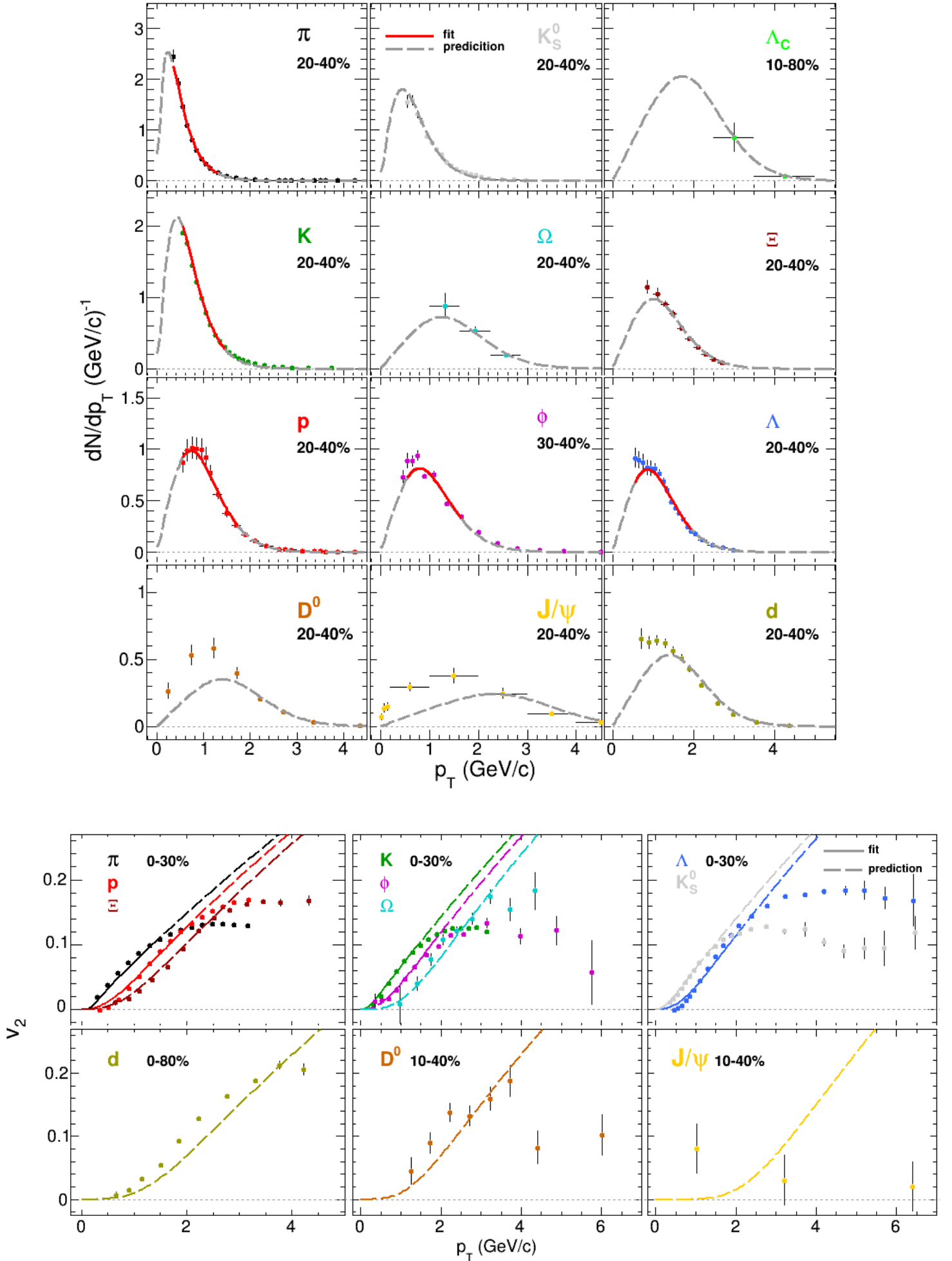Table 4: List of used data and centralities from 11.5 GeV Au-Au collisions.

Figure 14: Results of the simultaneous fit of particle spectra and v_2 at $\sqrt{s_{NN}} = 200$ GeV.

Unlike the previous fits, all of the fits done for $\sqrt{s_{NN}} = 200$ GeV and 11.5 GeV now consider pions, kaons, protons, phi and lambda particles in the fit using the fit ranges as listed in the tables above.

Starting with the fit at higher energies i.e. at 200 GeV, one can see in Figure **14** that especially the spectra of the lighter particles are described within the error bars for most data points with only a few showing deviations between one and two sigma. Unlike the previous fit at 2.76 TeV, the pion spectrum is now described without any significant deviations.

The Λ, J/ψ, D^0 and deuterons are described at higher p_T with large deviations for $p_T < 2\,\text{GeV/c}$ of up to four sigma for most of the data points except for the J/ψ which show significantly larger deviations. Similar to the deuterons where a proper description is not necessarily expected, it is also not known whether the D^0 and J/ψ should be able to be described by the blast-wave model since they include heavier charm quarks whose thermalization is still a subject of current research [63]. The elliptic flow shows a very similar behavior with well described flows for lighter particles at low p_T showing less than one sigma deviation from the fit and only the previously mentioned particles, which also show deviations for the particle spectra, once again show deviations of two to three sigma.

All in all a good description of both particle spectra and elliptic flow is possible with the *fos* blast-wave model at $\sqrt{s_{NN}} = 200$ GeV.

From the resulting fit parameters listed in Table **3** one can see that they show a very similar behavior as in the previous case with ρ_2 and R_x/R_y being almost identical and T_{kin} and ρ_0 in- or decreasing slightly for the different fits.

$\sqrt{s_{NN}} = 200$ GeV	T_{kin} (GeV)	ρ_0	ρ_2	R_x/R_y
π, K, p, ϕ, λ with feeddown	0.122 ± 0.000	0.899 ± 0.000	0.044 ± 0.000	0.907 ± 0.000
π, K, p, ϕ, λ without feeddown	0.115 ± 0.000	0.897 ± 0.002	0.042 ± 0.000	0.908 ± 0.000
K, p, ϕ, λ with feeddown	0.139 ± 0.001	0.835 ± 0.002	0.051 ± 0.000	0.912 ± 0.001
K, p, ϕ, λ without feeddown	0.128 ± 0.001	0.848 ± 0.003	0.047 ± 0.000	0.909 ± 0.001

Table 5: Fit parameters from *fos* blast-wave model fits at $\sqrt{s_{NN}} = 200$ GeV with- and without feeddown and in- or excluding pions.
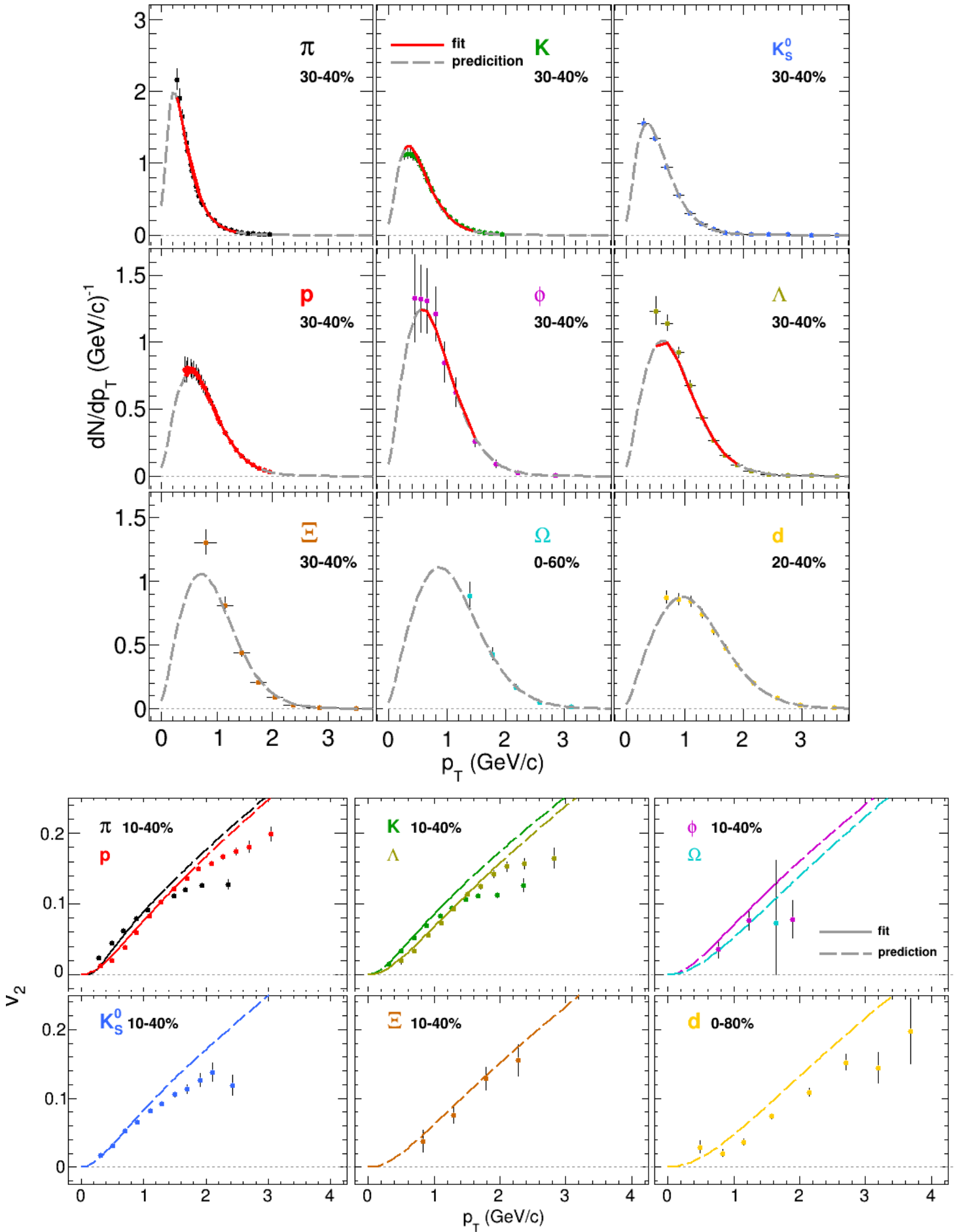
11.5 GeV Au-Au collision

Figure 15: Results of the simultaneous fit of particle spectra and v_2 at $\sqrt{s_{NN}} = 11.5$ GeV.

Continuing with the fits for data at 11.5 GeV shown in Figure **15**, one can see that a similar behavior to the previous fits is found. The majority of particle spectra are described by the fits with deviations smaller than one sigma for most data points with only a few points at $p_\mathrm{T} < 1.5$ GeV/c showing larger deviations of one to three sigma for π, Λ and Ξ particles.

Unlike the previous fit at 200 GeV, the pion spectrum once again shows some deviations for lower p_T here. They are, however, only slightly greater than one sigma and as such not that significant when compared to those from the 2.76 TeV fit. The fit of the elliptic flow agrees with the data at low p_T for basically all of the considered particles except for the deuterons which, as was mentioned before, are not necessarily expected to be described properly.

The resulting fit parameters listed in Table **6** show the exact same behavior when feeddown is included as those from previous fits with only slight changes for all of them.

$\sqrt{s_{NN}} = 11.5$ GeV	T_{kin} (GeV)	ρ_0	ρ_2	R_x/R_y
π, K, p, ϕ, λ with feeddown	0.127 ± 0.000	0.626 ± 0.002	0.038 ± 0.001	0.831 ± 0.002
π, K, p, ϕ, λ without feeddown	0.122 ± 0.000	0.619 ± 0.001	0.037 ± 0.001	0.833 ± 0.002
K, p, ϕ, λ with feeddown	0.157 ± 0.001	0.520 ± 0.003	0.044 ± 0.002	0.792 ± 0.006
K, p, ϕ, λ without feeddown	0.146 ± 0.000	0.524 ± 0.001	0.040 ± 0.000	0.791 ± 0.001

Table 6: Fit parameters from *fos* blast-wave model fits at $\sqrt{s_{NN}} = 11.5$ GeV with- and without feeddown and in- or excluding pions.

4.2 Simultaneous fits using the *boost* blast-wave model

As shown in the previous two sections, feeddown contributions only have a small effect on the shape of the particle spectra. Due to this a different approach to improve the description of the pion spectrum had to be found which is why a different version of the blast-wave model, the *boost* model, was formulated. To allow for a direct comparison of the results from the fits using the *fos* and *boost* blast-wave models the exact same data and fit ranges that were listed in Table **1**, **3** and **4** are used for the following *boost* model fits.

In Figure **16** the results of the *boost* blast-wave fit at 2.76 TeV is shown for both the particle spectra and elliptic flow with the resulting fit parameters listed in Table **7**.

$\sqrt{s_{NN}} = 2.76$ TeV	T_{kin} (GeV)	ρ_0	ρ_2	R_x/R_y
π, K, p with feeddown	0.097 ± 0.000	1.356 ± 0.001	0.097 ± 0.001	0.788 ± 0.001
π, K, p without feeddown	0.095 ± 0.001	1.192 ± 0.009	0.086 ± 0.002	0.814 ± 0.003
K, p with feeddown	0.142 ± 0.007	1.244 ± 0.017	0.140 ± 0.010	0.774 ± 0.005
K, p without feeddown	0.114 ± 0.005	1.104 ± 0.014	0.098 ± 0.006	0.824 ± 0.004

Table 7: Fit parameters from *boost* blast-wave model fits at $\sqrt{s_{NN}} = 2.76$ TeV with- and without feeddown and in- or excluding pions.

One can see that the fit parameters with feeddown are now more different compared to before. Unlike the *fos* blast-wave model where both ρ_2 and R_x/R_y were very similar for the different fits, one can now see that ρ_2 increases and R_x/R_y decreases for the fits including feeddown.

The fit results shown in Figure **16** show good descriptions of most particle spectra with the only exceptions being the same particles that could not be described completely using the *fos* version either. The most notable difference is that the pion spectrum is now described over the full p_T range, including, for the first time, very low p_T values. Compared to the deviations of approximately two sigma from the *fos* blast-wave fit the *boost* blast-wave model now gives a description which only deviates by slightly more than one sigma at most.

The elliptic flow of the different particles shows a similarly good description with most fits still describing the data within the errors with some data points which now show deviations slightly larger than one sigma. To get a better look at the differences of the two different blast-wave models a more direct comparison will be done in section **4.3**.
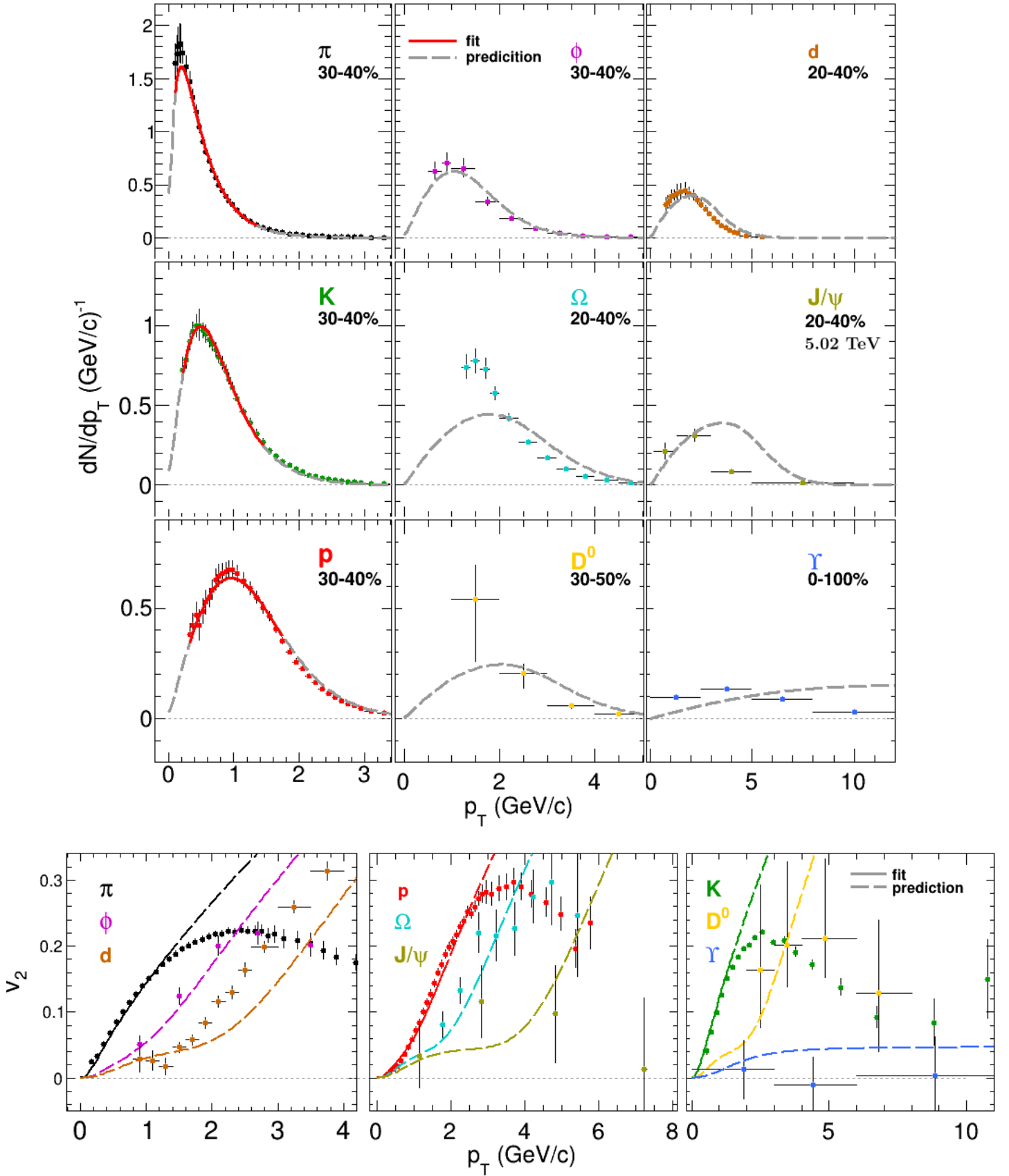
2.76 TeV Pb-Pb collision

Figure 16: Results of the simultaneous fit of particle spectra and v_2 using the *boost* blast-wave model at $\sqrt{s_{NN}} = 2.76$ TeV.
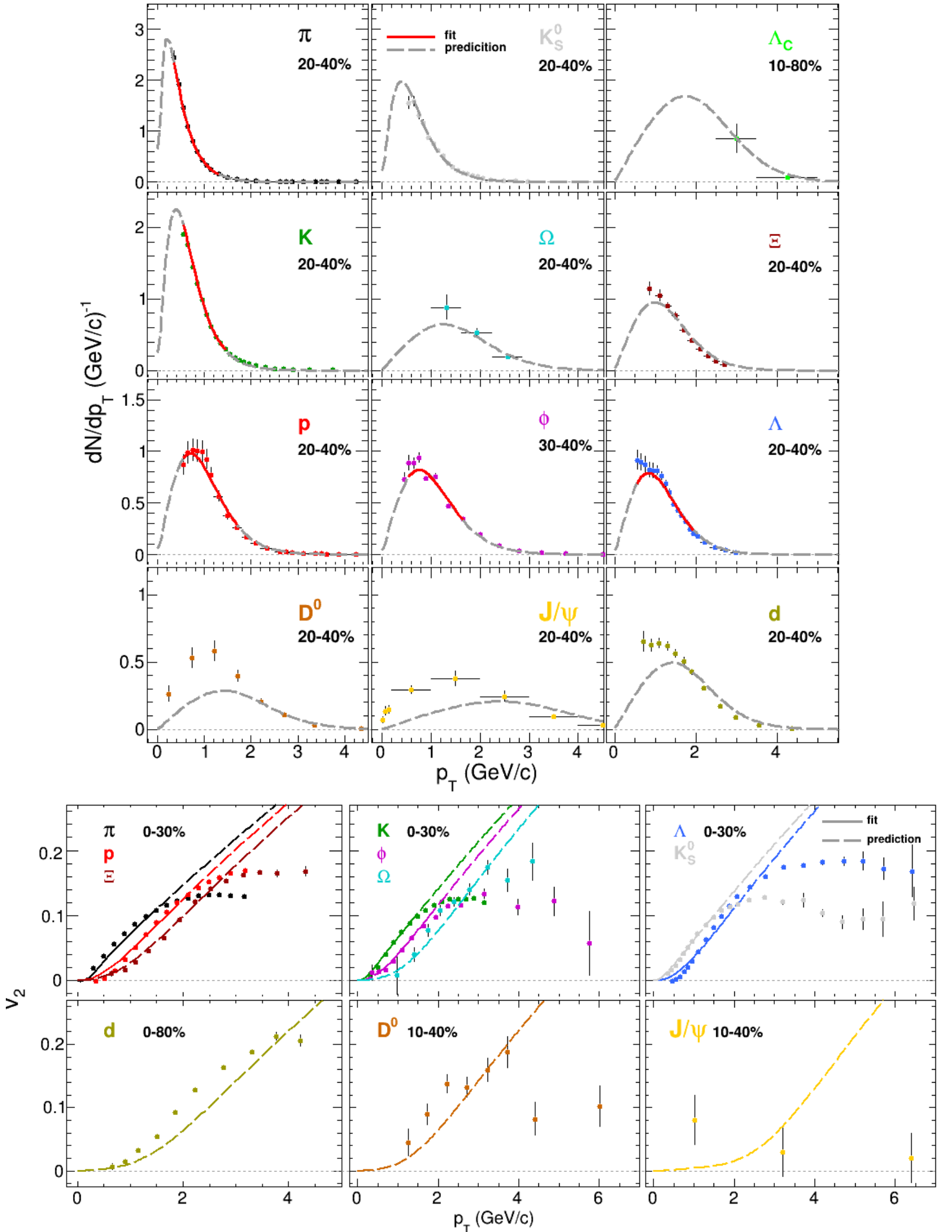
Figure 17: Results of the simultaneous fit of particle spectra and v_2 using the *boost* blast-wave model at $\sqrt{s_{NN}} = 200$ GeV.
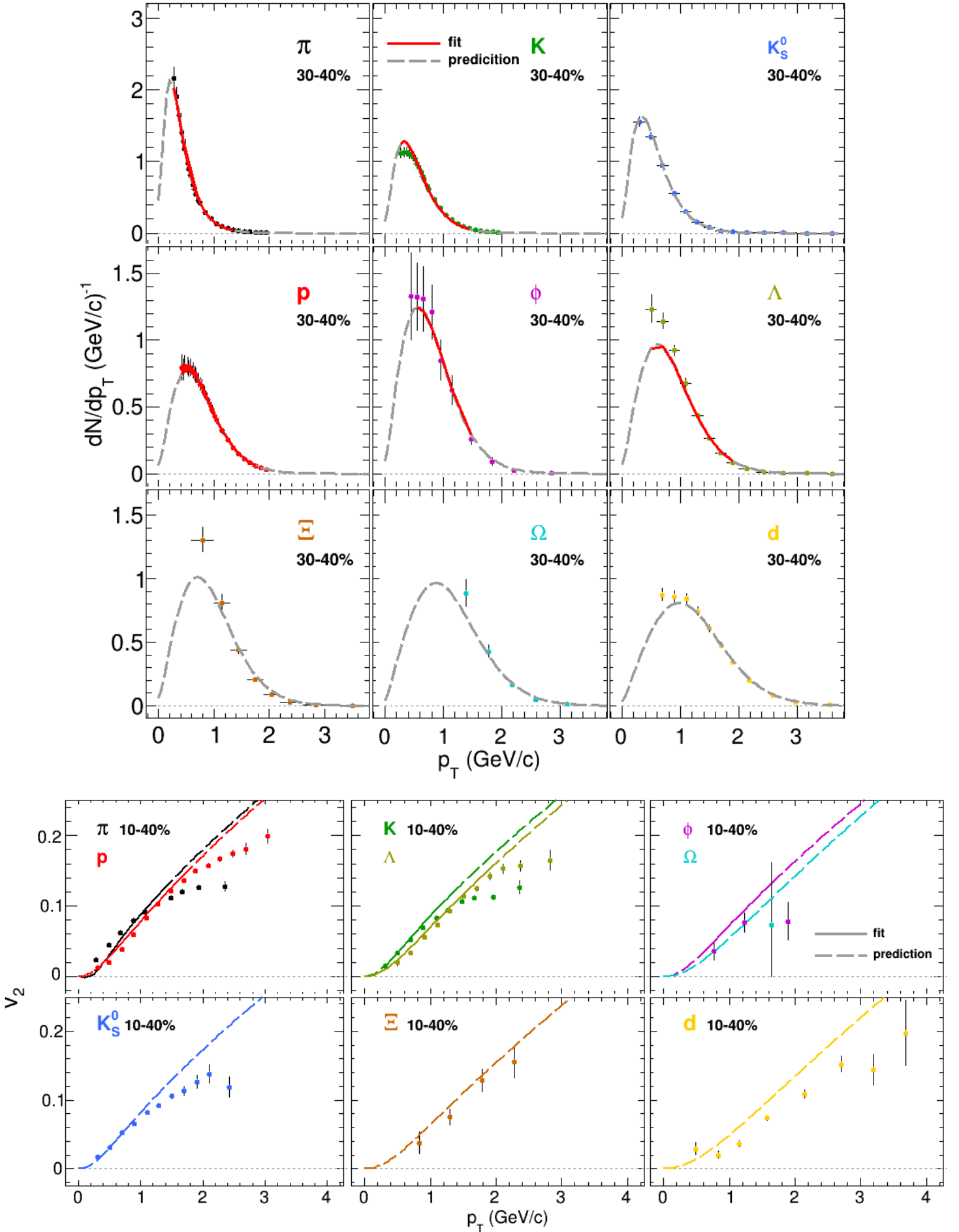
Figure 18: Results of the simultaneous fit of particle spectra and v_2 using the *boost* blast-wave model at $\sqrt{s_{NN}} = 11.5$ GeV.

For both fits using the *boost* blast-wave model at $\sqrt{s_{NN}} = 200$ GeV and $\sqrt{s_{NN}} = 11.5$ GeV shown in Figure **17** and **18** one sees that the fits using the *boost* blast-wave model resemble the *fos* fits. Most particle spectra show the same deviations they did for the *fos* blast-wave model fits while only showing small differences which will be looked at in more detail in section **4.3**. The only major difference of the fit using the *boost* blast-wave model is once again the description of the pion spectra. The fit of the pion spectrum at 200 GeV now shows a much more pronounced peak while the fit at 11.5 GeV is now able to describe the spectrum within the errors while the fit with the *fos* model showed deviations greater than one sigma.

The resulting fit parameters are listed in Table **8** and **9** for 200 GeV and 11.5 GeV respectively, showing changes of 10-20% for most of the different parameters.

$\sqrt{s_{NN}} = 200$ GeV	T_{kin} (GeV)	ρ_0	ρ_2	R_x/R_y
π, K, p, ϕ, Λ with feeddown	0.126 ± 0.000	1.007 ± 0.002	0.052 ± 0.000	0.884 ± 0.000
π, K, p, ϕ, Λ without feeddown	0.103 ± 0.000	0.978 ± 0.002	0.043 ± 0.000	0.897 ± 0.000
K, p, ϕ, Λ with feeddown	0.141 ± 0.001	0.941 ± 0.005	0.061 ± 0.001	0.888 ± 0.001
K, p, ϕ, Λ without feeddown	0.113 ± 0.001	0.920 ± 0.002	0.048 ± 0.000	0.900 ± 0.001

Table 8: Fit parameters from *boost* blast-wave model fits at $\sqrt{s_{NN}} = 200$ GeV with- and without feeddown and in- or excluding pions.

$\sqrt{s_{NN}} = 11.5$ GeV	T_{kin} (GeV)	ρ_0	ρ_2	R_x/R_y
π, K, p, ϕ, Λ with feeddown	0.129 ± 0.000	0.696 ± 0.002	0.043 ± 0.001	0.808 ± 0.002
π, K, p, ϕ, Λ without feeddown	0.118 ± 0.000	0.636 ± 0.001	0.034 ± 0.001	0.794 ± 0.003
K, p, ϕ, Λ with feeddown	0.163 ± 0.001	0.566 ± 0.004	0.041 ± 0.003	0.739 ± 0.008
K, p, ϕ, Λ without feeddown	0.142 ± 0.001	0.538 ± 0.003	0.032 ± 0.002	0.739 ± 0.007

Table 9: Fit parameters from *boost* blast-wave model fits at $\sqrt{s_{NN}} = 11.5$ GeV with- and without feeddown and in- or excluding pions.

4.3   Comparison of *fos* and *boost* blast-wave models

For a direct comparison of the two different models both fits using the *fos* and *boost* blast-wave models are now drawn in a single plot. In addition, the same fits in- or excluding pions are also drawn to check what kind of effect the pions have on the fits.

Unlike the prior plots the following comparisons do not depict the fitted ranges in the graph since they are the same as before for all of the different fits and do not provide any additional information for the comparison.
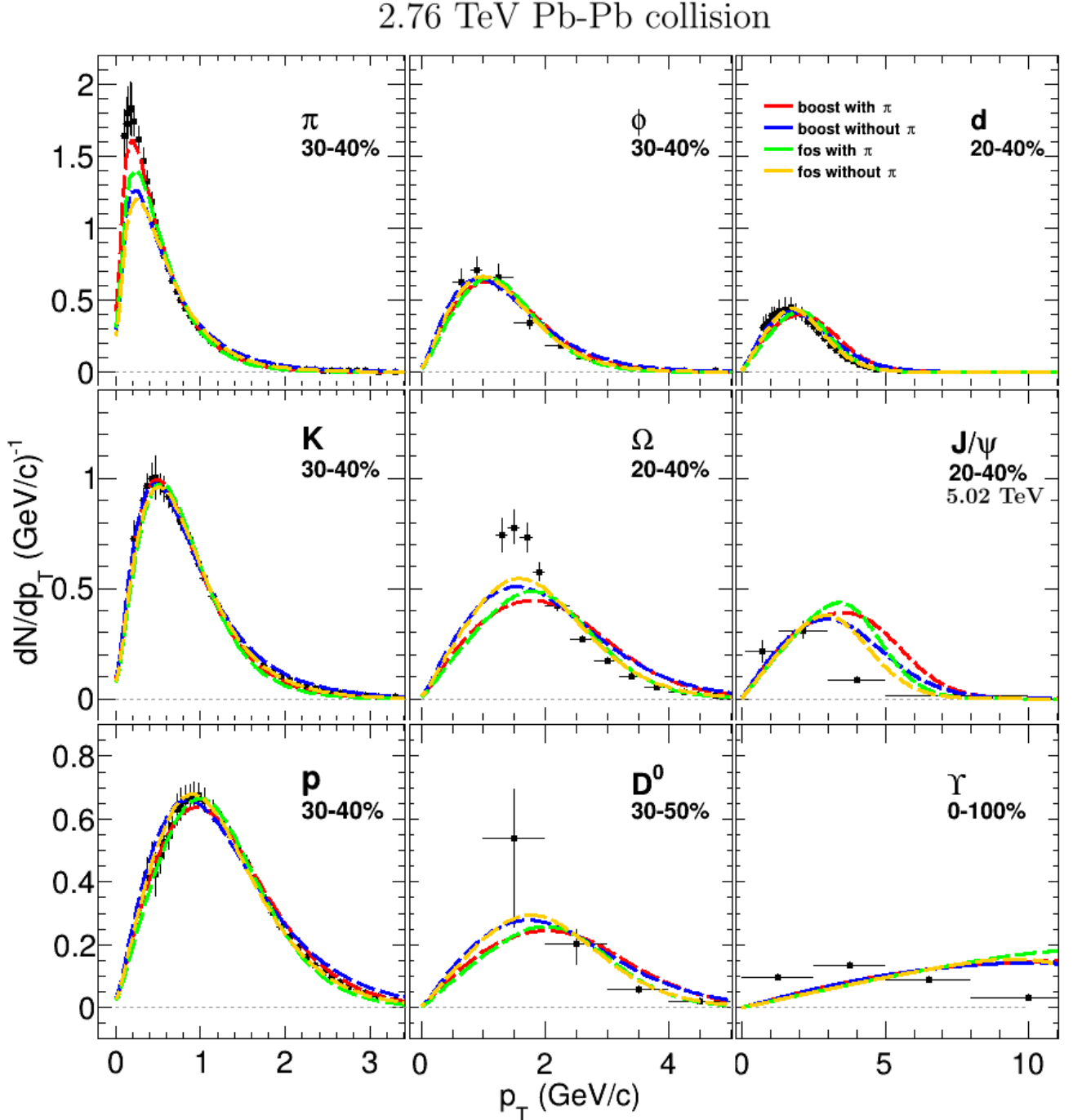

Figure 19: Comparison of fit results for particles spectra from the simultaneous fit for both *fos* and *boost* blast-wave models and in- or excluding pions at $\sqrt{s_{NN}} = 2.76$ TeV.
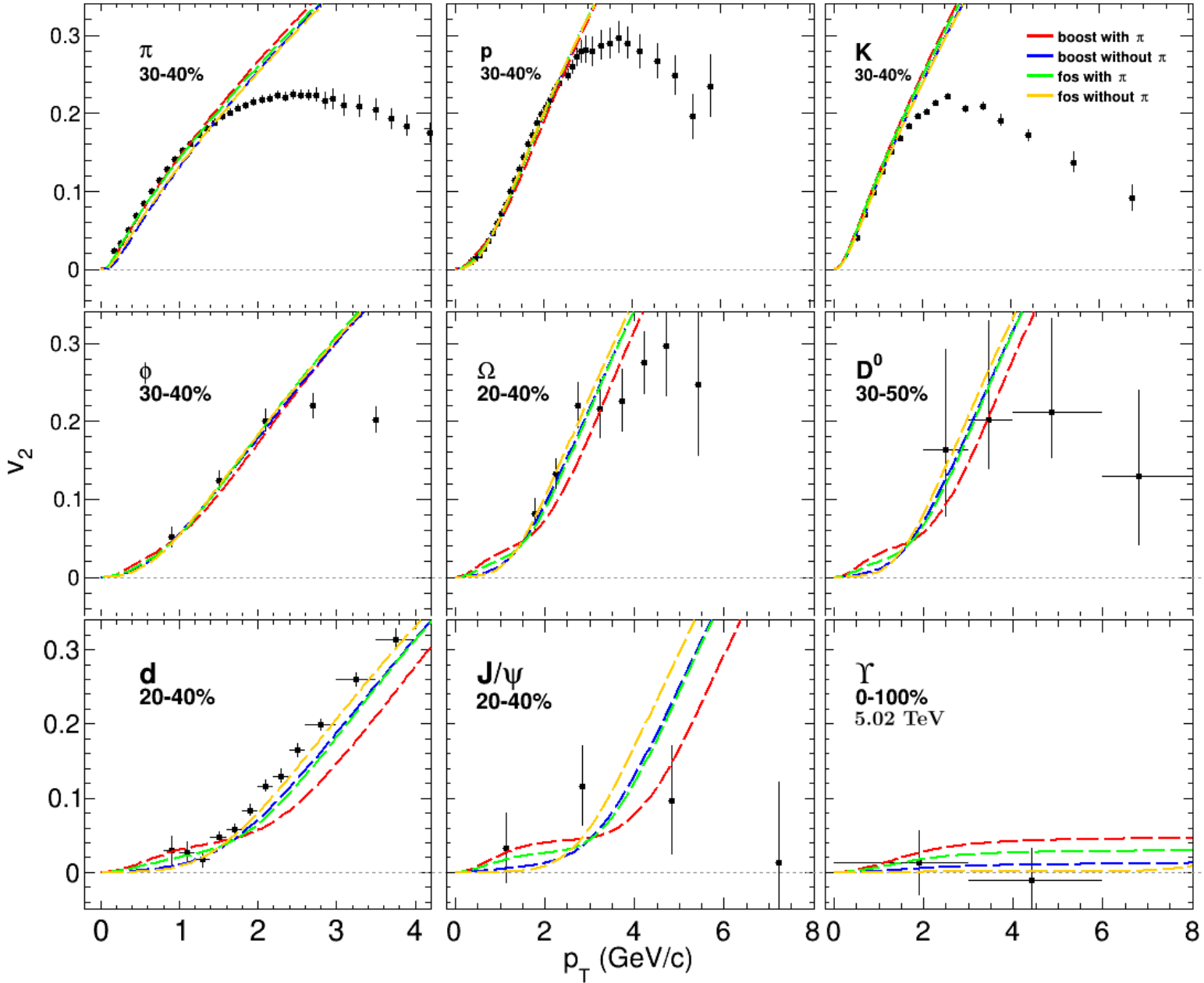
Figure 20: Comparison of the elliptic flow v_2 resulting from the simultaneous fit for both *boost* and *fos* versions of the blast-wave model in- or excluding pions at $\sqrt{s_{NN}} = 2.76$ TeV.

The most significant change for the particle spectra, shown in Figure **19**, is that the description of the pions improves significantly when using the *boost* blast-wave model compared to the *fos* version. For all the other particles the differences are only minor where the greatest differences are shown by those particles which already show larger deviations from the data.

The elliptic flow of the different particles is almost identical at low p_T for the lighter particles and splits up more with increasing mass. For the particles with higher masses one can also see that this splitting leads to the development of a constant elliptic flow covering increasingly higher ranges of p_T if the pions are included in the fit.

As a conclusion one can see that the *boost* blast-wave model including feeddown is able to describe the pion spectrum properly while the description of all other particles is just as good as it was using the *fos* model.

$\sqrt{s_{NN}} = 2.76$ TeV	T_{kin} (GeV)	ρ_0	ρ_2	R_x/R_y
fos with π	0.096 ± 0.014	1.180 ± 0.040	0.075 ± 0.007	0.829 ± 0.008
fos without π	0.135 ± 0.007	1.080 ± 0.016	0.097 ± 0.006	0.883 ± 0.004
boost with π	0.097 ± 0.001	1.356 ± 0.001	0.097 ± 0.001	0.788 ± 0.001
boost without π	0.157 ± 0.010	1.237 ± 0.013	0.143 ± 0.012	0.773 ± 0.006

Table 10: Fit parameters for *boost* and *fos* blast-wave model at $\sqrt{s_{NN}} = 2.76$ TeV.

Comparing the fit parameters of the *boost* and *fos* blast-wave model listed in Table **7** one can see that the *boost* blast-wave model gives higher values for ρ_0 and ρ_2 resulting in higher flow velocities. One can also see that the shape of the freeze-out surface is more elliptic when the *boost* blast-wave model is used since R_x/R_y decreases. Finally, while the *boost* blast-wave models describes the pions significantly better when they are included in the fit, one can see that their inclusion still has a significant effect on all of the parameters. Especially the kinetic freeze-out temperature is expected to be much lower when pions are included, decreasing by about 30% for the *fos* model and 40% for the *boost* model.
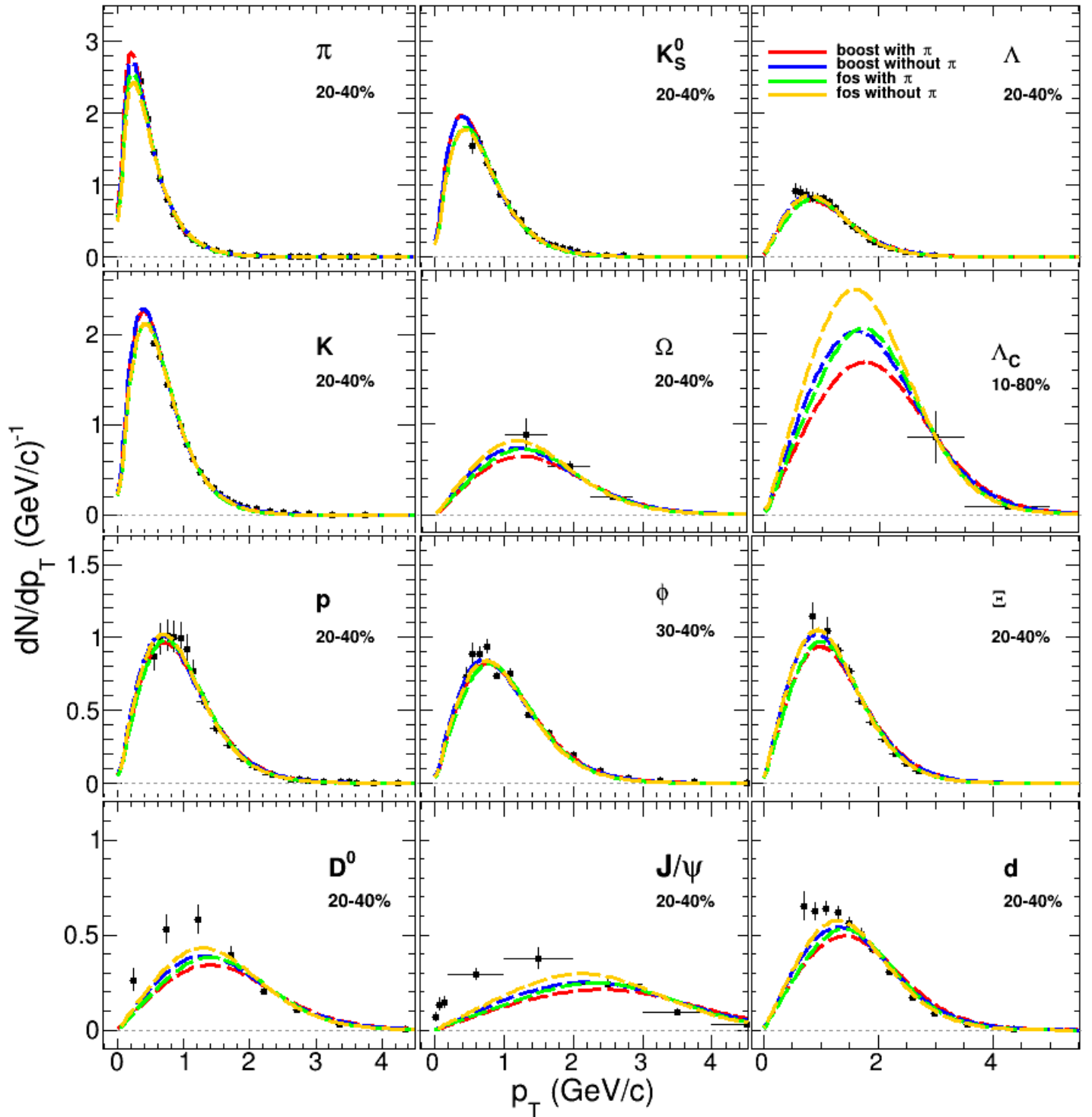
Figure 21: Comparison of fit results for particles spectra from the simultaneous fit for both *fos* and *boost* blast-wave models and in- or excluding pions at $\sqrt{s_{NN}} = 200$ GeV.
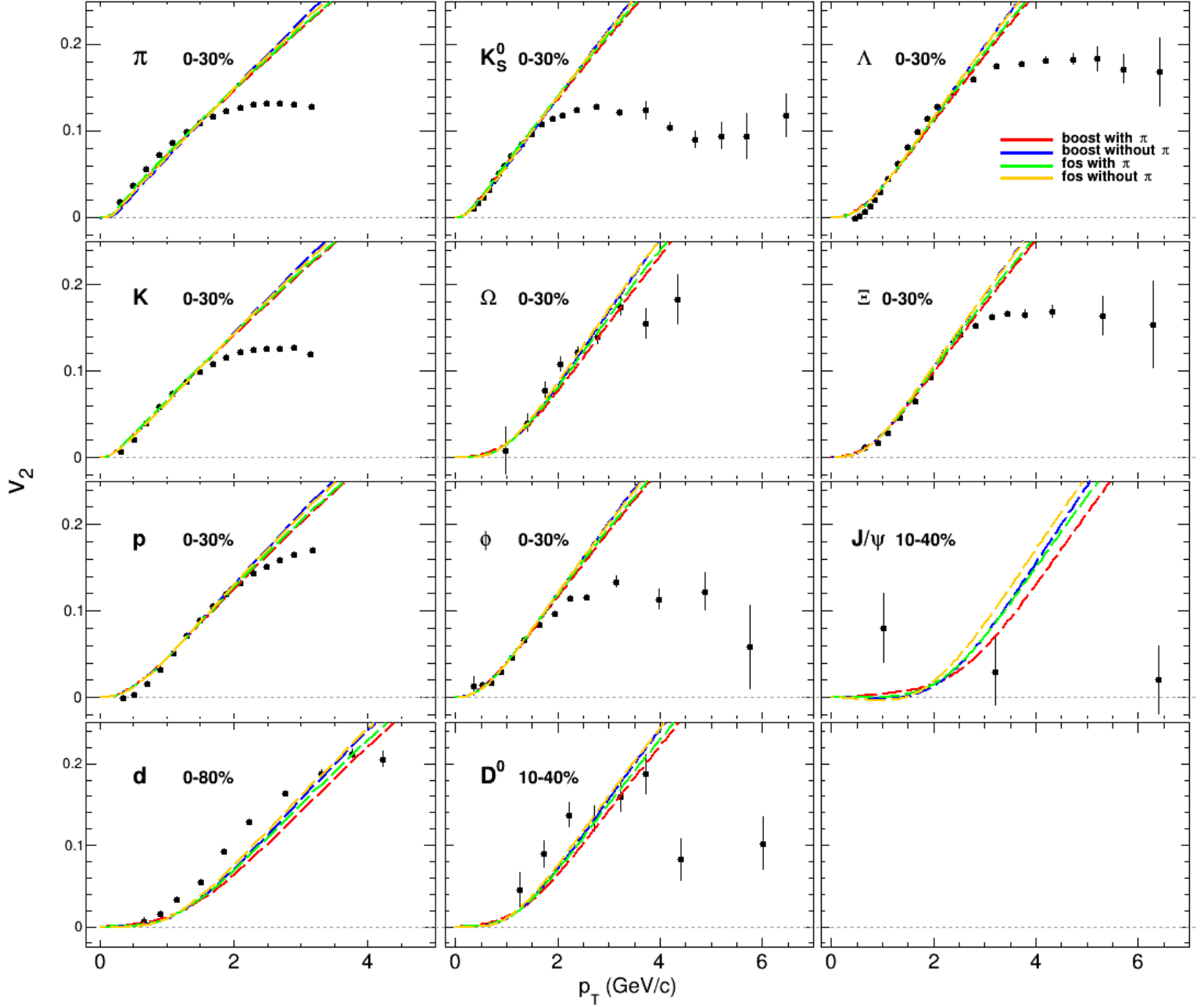
Figure 22: Comparison of the elliptic flow v_2 resulting from the simultaneous fit for both *boost* and *fos* versions of the blast-wave model in- or excluding pions at $\sqrt{s_{NN}} = 200$ GeV.
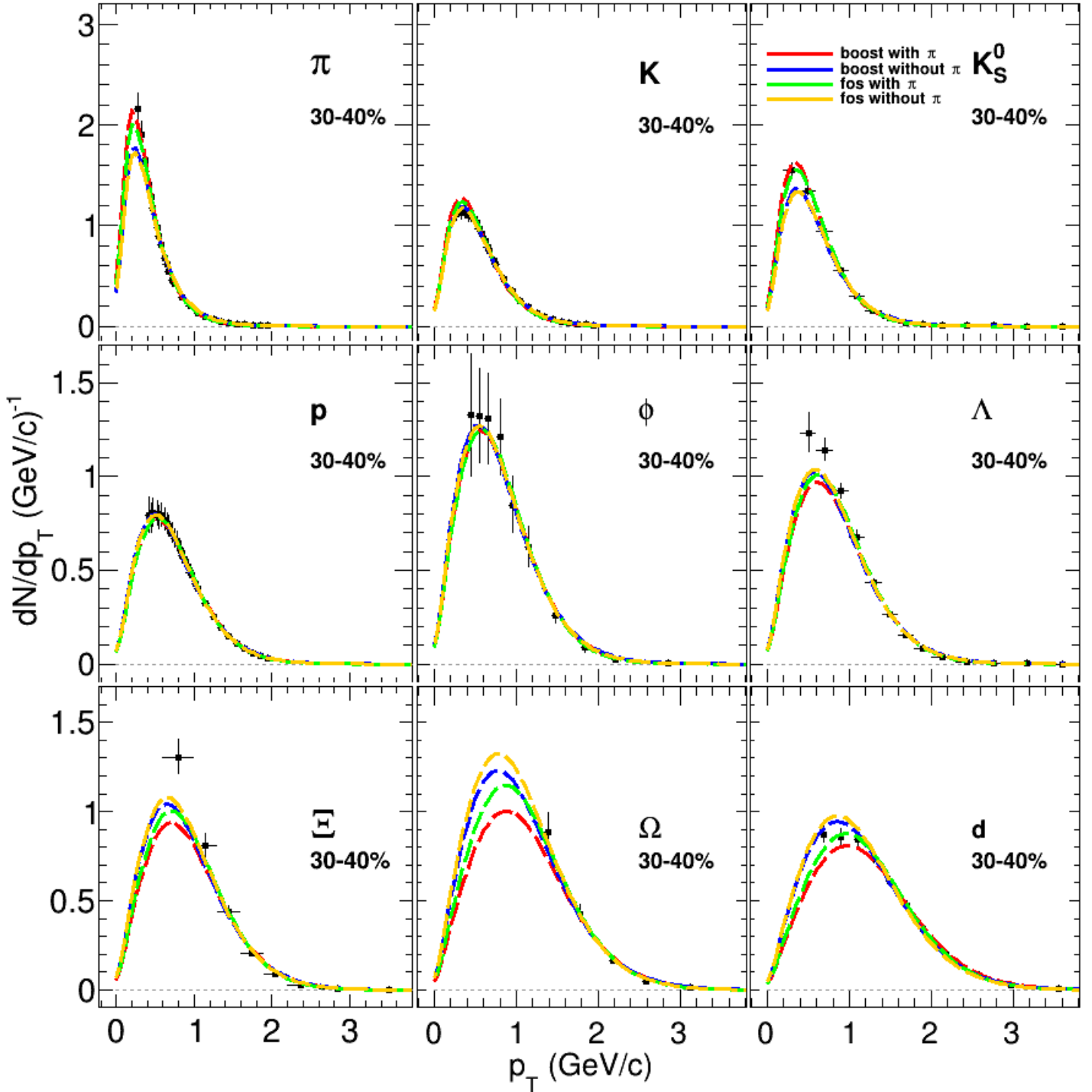
Figure 23: Comparison of fit results for particles spectra from the simultaneous fit for both *fos* and *boost* blast-wave models and in- or excluding pions at $\sqrt{s_{NN}} = 11.5$ GeV.
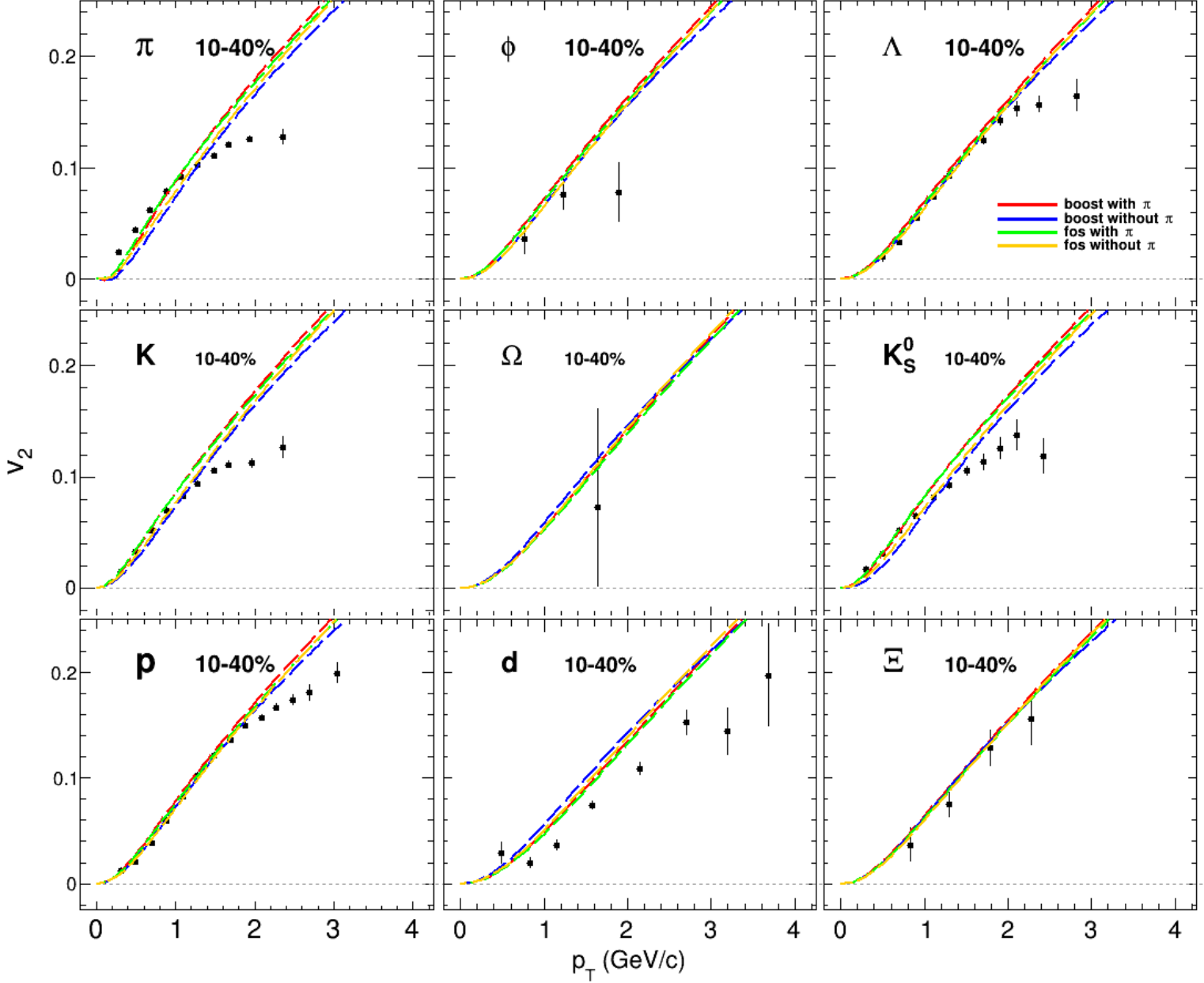
Figure 24: Comparison of the elliptic flow v_2 resulting from the simultaneous fit for both *boost* and *fos* versions of the blast-wave model in- or excluding pions at $\sqrt{s_{NN}} = 11.5$ GeV.

Both of the comparisons at $\sqrt{s_{NN}} = 200$ GeV and $\sqrt{s_{NN}} = 11.5$ shown in Figure **21**, **22**, **23** and **24** show very similar behaviors which is why both of them will be discussed here together. Just like for the fit at $\sqrt{s_{NN}} = 2.76$ TeV all particle spectra with fits that do not deviate much from the data show very similar descriptions for both the *fos* and *boost* blast-wave model. The particle spectra that change the most when different blast-wave models are used are those where less points of data are available giving them greater freedom in the fit. Focusing specifically on the pion spectra their description once again improves for 11.5 GeV while the peak for the fit at 200 GeV becomes more pronounced.

The elliptic flow also shows the same behavior as before with very similar fits for both models at low p_T splitting up more with increasing particle mass. Comparison of this splitting for the different center of mass energies shows that it is larger for higher collision energies.

In Table **11** and **12** the fit parameters are listed once again showing very similar behavior for the different fits as they did for the fits at $\sqrt{s_{NN}} = 2.76$ TeV. The parameters of the 200 GeV fit show much smaller changes since, unlike the other two fits, the *fos* blast-wave model was already able to describe the pion spectrum decreasing the effect of the *boost* model.

$\sqrt{s_{NN}} = 200$ GeV	T_{kin} (GeV)	ρ_0	ρ_2	R_x/R_y
fos with π	0.122 ± 0.000	0.899 ± 0.000	0.044 ± 0.000	0.907 ± 0.000
fos without π	0.139 ± 0.001	0.835 ± 0.001	0.051 ± 0.000	0.922 ± 0.001
boost with π	0.126 ± 0.000	1.007 ± 0.001	0.052 ± 0.000	0.884 ± 0.000
boost without π	0.141 ± 0.001	0.941 ± 0.005	0.061 ± 0.001	0.888 ± 0.001

Table 11: Fit parameters for *boost* and *fos* blast-wave model at $\sqrt{s_{NN}} = 200$ GeV.

$\sqrt{s_{NN}} = 11.5$ GeV	T_{kin} (GeV)	ρ_0	ρ_2	R_x/R_y
fos with π	0.127 ± 0.000	0.626 ± 0.002	0.038 ± 0.001	0.831 ± 0.002
fos without π	0.157 ± 0.001	0.520 ± 0.003	0.044 ± 0.002	0.792 ± 0.006
boost with π	0.129 ± 0.000	0.696 ± 0.002	0.043 ± 0.001	0.808 ± 0.001
boost without π	0.163 ± 0.001	0.566 ± 0.004	0.041 ± 0.003	0.739 ± 0.008

Table 12: Fit parameters for *boost* and *fos* blast-wave model at $\sqrt{s_{NN}} = 11.5$ GeV.

5 Conclusion and Outlook

In this thesis the effect of feeddown from resonance decays was studied using two different versions of the blast-wave model, namely the *fos* and *boost* models. From simultaneous blast-wave fits to particle spectra and elliptic flow it was found that the ratio of primary to total particles is a relatively flat function in transverse momentum (p_T) and as such has only a minor effect on the shape of the particle spectra and the elliptic flow v_2. For this reason all of the fits done at $\sqrt{s_{NN}} = 11.5, 200$ and 2760 GeV using the *fos* model look very similar to the fits where feeddown is not considered while only slightly affecting the resulting fit parameters. This means that all previously done fits that do not take feeddown contributions into account still give a good description of the particle spectra and elliptic flow.

Performing the exact same fits using the *boost* blast-wave model then made it possible to describe the pion spectra at low p_T showing an improved description of pion spectra for all different collision energies that were considered here. Comparison of the fits using the *fos* and *boost* blast-wave model showed that the *boost* model improved the description of the pion spectra while all the other particle spectra are mostly unaffected. With this it was shown that the *boost* blast-wave model including feeddown contributions is finally able to describe the deviations of pion particle spectra at low p_T which have usually been assumed to be caused mostly by feeddown effects.

Although the *boost* blast-wave model allows for a much better description of the pions, there are still deviations for some of the other particles. The most significant deviations are shown by J/ψ and D^0 particles which consist of heavier charm quarks of which it is not known whether they fully thermalize and also deuterons which are a molecular-like state of hadrons since they consist of both a neutron and a proton. This makes these particles very different from all the other particles that were considered here which is why a perfect description of these particles is not necessarily expected.

In all of the fits presented in this thesis it was assumed that the particle yields are proportional to the equilibrium densities in a non-interacting hadron gas. Here the Boltzmann approximation was used, possibly allowing for a better description of the different particles if a bose-distribution is used for the mesons and a fermi-distribution is used for the baryons. In addition, it was also assumed that the chemical potential $\mu \approx 0$ which is only a reasonable assumption for higher energy collisions as shown in [64]. Consequently, using a non-vanishing chemical potential for lower energy collisions could lead to an improvement of the description of the particle spectra. Finally an analysis of the differences between particles and anti-particles could prove to be interesting since a difference in their behavior is expected at lower energies and all of the results presented here only considered particles.

Bibliography

[1] G. Aad et al. "Observation of a new particle in the search for the Standard Model Higgs boson with the ATLAS detector at the LHC". In: *Physics Letters B* 716.1 (Sept. 2012), pp. 1–29. ISSN: 0370-2693. DOI: `10.1016/j.physletb.2012.08.020`. URL: `http://dx.doi.org/10.1016/j.physletb.2012.08.020`.

[2] S. Chatrchyan et al. "Observation of a new boson at a mass of 125 GeV with the CMS experiment at the LHC". In: *Physics Letters B* 716.1 (Sept. 2012), pp. 30–61. ISSN: 0370-2693. DOI: `10.1016/j.physletb.2012.08.021`. URL: `http://dx.doi.org/10.1016/j.physletb.2012.08.021`.

[3] Salvatore Rappoccio. "The experimental status of direct searches for exotic physics beyond the standard model at the Large Hadron Collider". In: *Reviews in Physics* 4 (Nov. 2019), p. 100027. ISSN: 2405-4283. DOI: `10.1016/j.revip.2018.100027`. URL: `http://dx.doi.org/10.1016/j.revip.2018.100027`.

[4] D. Boyanovsky, H.J. de Vega, and D.J. Schwarz. "Phase Transitions in the Early and Present Universe". In: *Annual Review of Nuclear and Particle Science* 56.1 (Nov. 2006), pp. 441–500. ISSN: 1545-4134. DOI: `10.1146/annurev.nucl.56.080805.140539`. URL: `http://dx.doi.org/10.1146/annurev.nucl.56.080805.140539`.

[5] Betty Abelev et al. "Centrality dependence of π, K, p production in Pb-Pb collisions at $\sqrt{s_{NN}} = 2.76$ TeV". In: *Phys. Rev.* C88 (2013), p. 044910. DOI: `10.1103/PhysRevC.88.044910`. arXiv: `1303.0737 [hep-ex]`.

[6] X. Sun et al. "Blast Wave Fits to Elliptic Flow Data at $\sqrt{s_{NN}} = 7.7$–2760 GeV". In: *Phys. Rev.* C91.2 (2015), p. 024903. DOI: `10.1103/PhysRevC.91.024903`. arXiv: `1410.1947 [hep-ph]`.

[7] Ekkard Schnedermann, Josef Sollfrank, and Ulrich W. Heinz. "Fireball spectra". In: *NATO Sci. Ser. B* 303 (1993), pp. 175–206.

[8] Ekkard Schnedermann, Josef Sollfrank, and Ulrich W. Heinz. "Thermal phenomenology of hadrons from 200-A/GeV S+S collisions". In: *Phys. Rev.* C48 (1993), pp. 2462–2475. DOI: `10.1103/PhysRevC.48.2462`. arXiv: `nucl-th/9307020 [nucl-th]`.

[9] C. Adler et al. "Identified Particle Elliptic Flow inAu+AuCollisions atsNN=130GeV". In: *Physical Review Letters* 87.18 (Oct. 2001). ISSN: 1079-7114. DOI: `10.1103/physrevlett.87.182301`. URL: `http://dx.doi.org/10.1103/PhysRevLett.87.182301`.

[10] Min He, Rainer J. Fries, and Ralf Rapp. "Scaling of Elliptic Flow, Recombination and Sequential Freeze-Out of Hadrons in Heavy-Ion Collisions". In: *Phys. Rev.* C82 (2010), p. 034907. DOI: `10.1103/PhysRevC.82.034907`. arXiv: `1006.1111 [nucl-th]`.

[11] B. I. Abelev et al. "Systematic Measurements of Identified Particle Spectra in pp, d^+ Au and Au+Au Collisions from STAR". In: *Phys. Rev.* C79 (2009), p. 034909. DOI: `10.1103/PhysRevC.79.034909`. arXiv: `0808.2041 [nucl-ex]`.

[12] Shreyasi Acharya et al. "Production of charged pions, kaons and (anti-)protons in Pb-Pb and inelastic pp collisions at $\sqrt{s_{\mathrm{NN}}} = 5.02$ TeV". In: *Phys. Rev. C* 101.4 (2020), p. 044907. DOI: 10.1103/PhysRevC.101.044907. arXiv: 1910.07678 [nucl-ex].

[13] Vardan Khachatryan et al. "Multiplicity and rapidity dependence of strange hadron production in pp, pPb, and PbPb collisions at the LHC". In: *Phys. Lett.* B768 (2017), pp. 103–129. DOI: 10.1016/j.physletb.2017.01.075. arXiv: 1605.06699 [nucl-ex].

[14] *Standard model of elementary particles.* [Online; accessed August 01, 2020]. 2010. URL: https://commons.wikimedia.org/wiki/File:Standard_Model_of_Elementary_Particles.svg.

[15] K.A. Olive. "Review of Particle Physics". In: *Chinese Physics C* 40.10 (Oct. 2016), p. 100001. DOI: 10.1088/1674-1137/40/10/100001. URL: https://doi.org/10.1088%2F1674-1137%2F40%2F10%2F100001.

[16] J. C. Collins and M. J. Perry. "Superdense Matter: Neutrons or Asymptotically Free Quarks?" In: *Phys. Rev. Lett.* 34 (21 May 1975), pp. 1353–1356. DOI: 10.1103/PhysRevLett.34.1353. URL: https://link.aps.org/doi/10.1103/PhysRevLett.34.1353.

[17] Reinhard Stock. "Relativistic Nucleus-Nucleus Collisions and the QCD Matter Phase Diagram". In: *Landolt-Börnstein - Group I Elementary Particles, Nuclei and Atoms* (2008), pp. 225–315. ISSN: 1616-9522. DOI: 10.1007/978-3-540-74203-6_7. URL: http://dx.doi.org/10.1007/978-3-540-74203-6_7.

[18] Anton Andronic et al. "Decoding the phase structure of QCD via particle production at high energy". In: *Nature* 561.7723 (2018), pp. 321–330. DOI: 10.1038/s41586-018-0491-6. arXiv: 1710.09425 [nucl-th].

[19] DEREK A. TEANEY. "VISCOUS HYDRODYNAMICS AND THE QUARK GLUON PLASMA". In: *Quark-Gluon Plasma 4* (Feb. 2010), pp. 207–266. DOI: 10.1142/9789814293297_0004. URL: http://dx.doi.org/10.1142/9789814293297_0004.

[20] A. M. Poskanzer and S. A. Voloshin. "Methods for analyzing anisotropic flow in relativistic nuclear collisions". In: *Physical Review C* 58.3 (Sept. 1998), pp. 1671–1678. ISSN: 1089-490X. DOI: 10.1103/physrevc.58.1671. URL: http://dx.doi.org/10.1103/PhysRevC.58.1671.

[21] Raimond Snellings. "Elliptic flow: a brief review". In: *New Journal of Physics* 13.5 (May 2011), p. 055008. ISSN: 1367-2630. DOI: 10.1088/1367-2630/13/5/055008. URL: http://dx.doi.org/10.1088/1367-2630/13/5/055008.

[22] Peter F. Kolb, Josef Sollfrank, and Ulrich Heinz. "Anisotropic transverse flow and the quark-hadron phase transition". In: *Physical Review C* 62.5 (Oct. 2000). ISSN: 1089-490X. DOI: 10.1103/physrevc.62.054909. URL: http://dx.doi.org/10.1103/PhysRevC.62.054909.

[23] P. Huovinen et al. "Radial and elliptic flow at RHIC: further predictions". In: *Physics Letters B* 503.1-2 (Mar. 2001), pp. 58–64. ISSN: 0370-2693. DOI: `10.1016/s0370-2693(01)00219-2`. URL: `http://dx.doi.org/10.1016/S0370-2693(01)00219-2`.

[24] L. Adamczyk et al. "Centrality dependence of identified particle elliptic flow in relativistic heavy ion collisions at $\sqrt{s_{NN}}$=7.7–62.4 GeV". In: *Phys. Rev.* C93.1 (2016), p. 014907. DOI: `10.1103/PhysRevC.93.014907`. arXiv: `1509.08397 [nucl-ex]`.

[25] Taesoo Song et al. "J/ψ production and elliptic flow in relativistic heavy-ion collisions". In: *Phys. Rev.* C83 (2011), p. 014914. DOI: `10.1103/PhysRevC.83.014914`. arXiv: `1008.2730 [hep-ph]`.

[26] Klaus Reygers et al. "Blast-wave description of Υ elliptic flow at energies available at the CERN Large Hadron Collider". In: *Physical Review C* 101.6 (June 2020). ISSN: 2469-9993. DOI: `10.1103/physrevc.101.064905`. URL: `http://dx.doi.org/10.1103/PhysRevC.101.064905`.

[27] Fabrice Retière and Michael Annan Lisa. "Observable implications of geometrical and dynamical aspects of freeze-out in heavy ion collisions". In: *Physical Review C* 70.4 (Oct. 2004). ISSN: 1089-490X. DOI: `10.1103/physrevc.70.044907`. URL: `http://dx.doi.org/10.1103/PhysRevC.70.044907`.

[28] *Private communication with Klaus Reygers*. 2020.

[29] Torbjorn Sjostrand, Stephen Mrenna, and Peter Z. Skands. "PYTHIA 6.4 Physics and Manual". In: *JHEP* 05 (2006), p. 026. DOI: `10.1088/1126-6708/2006/05/026`. arXiv: `hep-ph/0603175 [hep-ph]`.

[30] Torbjorn Sjostrand, Stephen Mrenna, and Peter Z. Skands. "A Brief Introduction to PYTHIA 8.1". In: *Comput. Phys. Commun.* 178 (2008), pp. 852–867. DOI: `10.1016/j.cpc.2008.01.036`. arXiv: `0710.3820 [hep-ph]`.

[31] R. Brun & F. Rademakers. *ROOT: An object oriented data analysis framework*. DOI: `10.1016/S0168-9002(97)00048-X`.

[32] F. James and M. Roos. "Minuit - a system for function minimization and analysis of the parameter errors and correlations". In: *Computer Physics Communications* 10.6 (1975), pp. 343–367. ISSN: 0010-4655. DOI: `https://doi.org/10.1016/0010-4655(75)90039-9`. URL: `http://www.sciencedirect.com/science/article/pii/0010465575900399`.

[33] *Private communication with Nadine Grünwald*. 2020.

[34] Jaroslav Adam et al. "Centrality dependence of the nuclear modification factor of charged pions, kaons, and protons in Pb-Pb collisions at $\sqrt{s_{NN}} = 2.76$ TeV". In: *Phys. Rev.* C93.3 (2016), p. 034913. DOI: `10.1103/PhysRevC.93.034913`. arXiv: `1506.07287 [nucl-ex]`.

[35] Jaroslav Adam et al. "K$^*(892)^0$ and $\phi(1020)$ meson production at high transverse momentum in pp and Pb-Pb collisions at $\sqrt{s_{NN}} = 2.76$ TeV". In: *Phys. Rev.* C95.6 (2017), p. 064606. DOI: `10.1103/PhysRevC.95.064606`. arXiv: `1702.00555 [nucl-ex]`.

[36] Betty Bezverkhny Abelev et al. "Multi-strange baryon production at mid-rapidity in Pb-Pb collisions at $\sqrt{s_{NN}}$ = 2.76 TeV". In: *Phys. Lett.* B728 (2014). [Erratum: Phys. Lett.B734,409(2014)], pp. 216–227. DOI: 10.1016/j.physletb.2014.05.052,10.1016/j.physletb.2013.11.048. arXiv: 1307.5543 [nucl-ex].

[37] Jaroslav Adam et al. "Transverse momentum dependence of D-meson production in Pb-Pb collisions at $\sqrt{s_{NN}}$ = 2.76 TeV". In: *JHEP* 03 (2016), p. 081. DOI: 10.1007/JHEP03(2016)081. arXiv: 1509.06888 [nucl-ex].

[38] Jaroslav Adam et al. "Production of light nuclei and anti-nuclei in pp and Pb-Pb collisions at energies available at the CERN Large Hadron Collider". In: *Phys. Rev.* C93.2 (2016), p. 024917. DOI: 10.1103/PhysRevC.93.024917. arXiv: 1506.08951 [nucl-ex].

[39] Shreyasi Acharya et al. "Measurement of deuteron spectra and elliptic flow in Pb–Pb collisions at $\sqrt{s_{NN}}$ = 2.76 TeV at the LHC". In: *Eur. Phys. J.* C77.10 (2017), p. 658. DOI: 10.1140/epjc/s10052-017-5222-x. arXiv: 1707.07304 [nucl-ex].

[40] S. Acharya et al. "Centrality and transverse momentum dependence of inclusive J/Ψ production at midrapidity in Pb–Pb collisions at sNN=5.02 TeV". In: *Physics Letters B* 805 (June 2020), p. 135434. ISSN: 0370-2693. DOI: 10.1016/j.physletb.2020.135434. URL: http://dx.doi.org/10.1016/j.physletb.2020.135434.

[41] Vardan Khachatryan et al. "Suppression of $\Upsilon(1S), \Upsilon(2S)$ and $\Upsilon(3S)$ production in PbPb collisions at $\sqrt{s_{NN}}$ = 2.76 TeV". In: *Phys. Lett.* B770 (2017), pp. 357–379. DOI: 10.1016/j.physletb.2017.04.031. arXiv: 1611.01510 [nucl-ex].

[42] Betty Bezverkhny Abelev et al. "Elliptic flow of identified hadrons in Pb-Pb collisions at $\sqrt{s_{NN}}$ = 2.76 TeV". In: *JHEP* 06 (2015), p. 190. DOI: 10.1007/JHEP06(2015)190. arXiv: 1405.4632 [nucl-ex].

[43] B. Abelev et al. "D meson elliptic flow in non-central Pb-Pb collisions at $\sqrt{s_{NN}}$ = 2.76TeV". In: *Phys. Rev. Lett.* 111 (2013), p. 102301. DOI: 10.1103/PhysRevLett.111.102301. arXiv: 1305.2707 [nucl-ex].

[44] Ehab Abbas et al. "J/ψ Elliptic Flow in Pb-Pb Collisions at $\sqrt{s_{NN}}$ = 2.76 TeV". In: *Phys. Rev. Lett.* 111 (2013), p. 162301. DOI: 10.1103/PhysRevLett.111.162301. arXiv: 1303.5880 [nucl-ex].

[45] Shreyasi Acharya et al. "Measurement of Υ(1S) elliptic flow at forward rapidity in Pb-Pb collisions at $\sqrt{s_{NN}}$ = 5.02 TeV". In: (2019). arXiv: 1907.03169 [nucl-ex].

[46] L. Adamczyk et al. "Observation of an Energy-Dependent Difference in Elliptic Flow between Particles and Antiparticles in Relativistic Heavy Ion Collisions". In: *Physical Review Letters* 110.14 (Apr. 2013). ISSN: 1079-7114. DOI: 10.1103/physrevlett.110.142301. URL: http://dx.doi.org/10.1103/PhysRevLett.110.142301.

[47] STAR Collaboration. *Energy dependence of charged pion, proton and anti-proton transverse momentum spectra for Au+Au collisions at $\sqrt{s_N N}$ = 62.4 and 200 GeV*. 2007. arXiv: nucl-ex/0703040 [nucl-ex].

[48] A. Adare et al. "Spectra and ratios of identified particles in Au+Au andd+Au collisions atsNN=200GeV". In: *Physical Review C* 88.2 (Aug. 2013). ISSN: 1089-490X. DOI: 10.1103/physrevc.88.024906. URL: http://dx.doi.org/10.1103/PhysRevC.88.024906.

[49] B. I. Abelev et al. "Measurements of ϕ meson production in relativistic heavy-ion collisions at the BNL Relativistic Heavy Ion Collider (RHIC)". In: *Physical Review C* 79.6 (June 2009). ISSN: 1089-490X. DOI: 10.1103/physrevc.79.064903. URL: http://dx.doi.org/10.1103/PhysRevC.79.064903.

[50] G. Agakishiev et al. "Strangeness Enhancement in Cu-Cu and Au-Au Collisions atsNN=200 GeV". In: *Physical Review Letters* 108.7 (Feb. 2012). ISSN: 1079-7114. DOI: 10.1103/physrevlett.108.072301. URL: http://dx.doi.org/10.1103/PhysRevLett.108.072301.

[51] J. Adam et al. "Centrality and transverse momentum dependence of D0 -meson production at mid-rapidity in Au + Au collisions at sNN=200 GeV". In: *Physical Review C* 99.3 (Mar. 2019). ISSN: 2469-9993. DOI: 10.1103/physrevc.99.034908. URL: http://dx.doi.org/10.1103/PhysRevC.99.034908.

[52] J. Adam et al. "Beam energy dependence of (anti-)deuteron production in Au + Au collisions at the BNL Relativistic Heavy Ion Collider". In: *Physical Review C* 99.6 (June 2019). ISSN: 2469-9993. DOI: 10.1103/physrevc.99.064905. URL: http://dx.doi.org/10.1103/PhysRevC.99.064905.

[53] L. Adamczyk et al. "Energy dependence of J/ψ production in Au + Au collisions at sNN=39,62.4 and 200GeV". In: *Physics Letters B* 771 (Aug. 2017), pp. 13–20. ISSN: 0370-2693. DOI: 10.1016/j.physletb.2017.04.078. URL: http://dx.doi.org/10.1016/j.physletb.2017.04.078.

[54] J. Adam et al. "First Measurement of Λ_c Baryon Production in Au+Au Collisions at sNN=200 GeV". In: *Physical Review Letters* 124.17 (May 2020). ISSN: 1079-7114. DOI: 10.1103/physrevlett.124.172301. URL: http://dx.doi.org/10.1103/PhysRevLett.124.172301.

[55] L. Adamczyk et al. "Centrality and Transverse Momentum Dependence of Elliptic Flow of Multistrange Hadrons and Meson inAu+AuCollisions atsNN=200 GeV". In: *Physical Review Letters* 116.6 (Feb. 2016). ISSN: 1079-7114. DOI: 10.1103/physrevlett.116.062301. URL: http://dx.doi.org/10.1103/PhysRevLett.116.062301.

[56] L. Adamczyk et al. "Measurement of D0 Azimuthal Anisotropy at Midrapidity in Au+Au Collisions at sNN=200 GeV". In: *Physical Review Letters* 118.21 (May 2017). ISSN: 1079-7114. DOI: 10.1103/physrevlett.118.212301. URL: http://dx.doi.org/10.1103/PhysRevLett.118.212301.

[57] STAR Collaboration et al. *Measurement of elliptic flow of light nuclei at $\sqrt{s_{NN}} = 200, 62.4, 39, 27, 19.6, 11.5, and 7.7 GeV at RHIC*. 2016. arXiv: 1601.07052 [nucl-ex].

[58] L. Adamczyk et al. "Measurement of J/Ψ Azimuthal Anisotropy in Au+Au Collision at $\sqrt{s_{NN}} = 200$ GeV". In: *Physical Review Letters* 111.5 (Aug. 2013). ISSN: 1079-7114. DOI: 10.1103/physrevlett.111.052301. URL: http://dx.doi.org/10.1103/PhysRevLett.111.052301.

[59] L. Adamczyk et al. "Bulk properties of the medium produced in relativistic heavy-ion collisions from the beam energy scan program". In: *Physical Review C* 96.4 (Oct. 2017). ISSN: 2469-9993. DOI: 10.1103/physrevc.96.044904. URL: http://dx.doi.org/10.1103/PhysRevC.96.044904.

[60] L. Adamczyk et al. "Probing parton dynamics of QCD matter with Ω and ϕ production". In: *Physical Review C* 93.2 (Feb. 2016). ISSN: 2469-9993. DOI: 10.1103/physrevc.93.021903. URL: http://dx.doi.org/10.1103/PhysRevC.93.021903.

[61] STAR Collaboration et al. *Strange hadron production in Au+Au collisions at $\sqrt{s_{\mathrm{NN}}} = 7.7, 11.5, 19.6, 27,$ and 39 GeV*. 2019. arXiv: 1906.03732 [nucl-ex].

[62] L. Adamczyk et al. "Elliptic flow of identified hadrons in Au+Au collisions atsNN=7.7–62.4 GeV". In: *Physical Review C* 88.1 (July 2013). ISSN: 1089-490X. DOI: 10.1103/physrevc.88.014902. URL: http://dx.doi.org/10.1103/PhysRevC.88.014902.

[63] Nadine Grünwald. *Bachelor Arbeit: Simultaneous blast-wave description of transverse momentum spectra and elliptic fow data for $\sqrt{s_{NN}} = 7.7$ GeV - 5.02 TeV*. 2020.

[64] A. Andronic, P. Braun-Munzinger, and J. Stachel. *Thermal hadron production in relativistic nuclear collisions: the hadron mass spectrum, the horn, and the QCD phase transition*. 2008. arXiv: 0812.1186 [nucl-th].

Erklärung

Ich versichere, dass ich diese Arbeit selbstständig verfasst und keine anderen als die angegebenen Quellen und Hilfsmittel benutzt habe.

Heidelberg, den 28.08.2020,